Journal of Catalysis 279 (2011) 287–300

Contents lists available at ScienceDirect

Journal of Catalysis

journal homepage: www.elsevier.com/locate/jcat

"Redox" vs "associative formate with –OH group regeneration" WGS reaction mechanism on Pt/CeO_2: Effect of platinum particle size

Christos M. Kalamaras, Sofia Americanou, Angelos M. Efstathiou *

Department of Chemistry, Heterogeneous Catalysis Laboratory, University of Cyprus, P.O. Box 20537, CY 1678, Nicosia, Cyprus

ARTICLE INFO

Article history:
Received 14 October 2010
Revised 18 January 2011
Accepted 22 January 2011
Available online 2 March 2011

Keywords:
WGS reaction mechanism
Ceria-supported Pt
SSITKA-DRIFTS
SSITKA-MS
H_2-TPD

ABSTRACT

A series of *x* wt.% Pt/CeO_2 catalysts (*x* = 0.1–2.0) was prepared to investigate for the first time the effect of Pt particle size on important kinetic and mechanistic aspects of the water–gas shift (WGS) reaction, namely the concentration (μmol g^{-1}) and chemical structure of *active* adsorbed reaction intermediates present in the "carbon-path" and "hydrogen-path" of the WGS reaction at 300 °C. For this, steady-state isotopic transient kinetic analysis (SSITKA) coupled with *in situ* DRIFTS and mass spectrometry experiments was performed using D_2O and ^{13}CO. A novel transient isotopic experiment performed allowed to quantify the initial transient rates of reactions of adsorbed formate (–COOH) and CO by water, based on which it was concluded that formate should not be considered as an important intermediate. According to the present work, it is proposed that the WGS reaction on ceria-supported Pt at 300 °C occurs largely via the "*redox*" mechanism, and to a lesser extent via the "*associative formate with –OH group regeneration*" mechanism. The TOF (s^{-1}) of WGS was found to vary only slightly with Pt particle size (1.3–8.0 nm), while the specific reaction rate based on the length of periphery of Pt–CeO_2 interface (μmol cm^{-1} s^{-1}) was found to significantly increase with increasing platinum loading and mean particle size in the 250–300 °C range.

1. Introduction

There is an important need nowadays to improve the sustainability of the energy system worldwide given the perceived projected decline in petroleum resources in the near future combined with increasing political and environmental concerns about fossil fuels. The development of a hydrogen-based economy (H_2 being the energy carrier), a strategy for power production with significant advantages, appears to be a primary target [1,2]. Given these challenges, there is an important need to produce H_2 in an efficient and environmentally acceptable way and with minimum cost [3].

Water–gas shift (WGS) is an important industrial reaction in a number of chemical processes that produce H_2, including steam reforming of hydrocarbons (including natural gas), sugars, alcohols, and bio-oil [4–8]. The heterogeneously catalyzed WGS reaction is equilibrium limited and moderately exothermic ($CO + H_2O \leftrightarrow CO_2 + H_2$, $\Delta H^o = -41.2$ kJ/mol), where very low CO concentration levels can be achieved only at low temperatures ($T < 200$ °C).

Noble metals (e.g., Pt and Au) supported on reducible metal oxide carriers appear to be promising candidates for the low-temperature WGS reaction compared to the conventionally used Cu–Zn-based catalysts [8]. However, their stability under practical conditions is problematic and depends on the synthesis method employed [9]. There is an increasing demand for fundamental understanding of the LT-WGS catalytic reaction at the molecular level in order to achieve activity, selectivity, and stability optimization under industrial conditions by the design of suitably functional catalytic materials. In order to achieve this goal, it is of great importance to thoroughly investigate mechanistic aspects of the WGS reaction employing *in situ* spectroscopic and kinetic studies under reaction conditions (operando studies) [10].

Two main reaction mechanisms have been proposed in the literature: (i) the regenerative mechanism or *redox* [11–16] and (ii) the adsorptive or *associative* mechanism (non-redox) [17–21]. In the redox mechanism, CO adsorbs on the noble metal surface which then diffuses at the metal–support interface and reacts with lattice oxygen of support to form CO_2(g). Water adsorbs and dissociates mainly on the reduced support sites, thus re-oxidizing them and subsequently producing H_2(g). In the associative mechanism, CO and H_2O were proposed to adsorb on catalyst active sites to form a surface "carbon-containing" intermediate, e.g., formate, carbonate, or bicarbonate, which further reacts or decomposes to form H_2 and CO_2. The chemical nature of this active "carbon-containing" intermediate and its true site location, e.g., support, metal–support interface, or metal surface still remain controversial issues. Pierre et al. [22] and recently Zhai et al. [23] have provided strong experimental evidence that Pt- or Au-oxidized species (e.g., Pt–OH_x)

* Corresponding author. Fax: +357 22 892801.
E-mail address: efstath@ucy.ac.cy (A.M. Efstathiou).

0021-9517/$ - see front matter © 2011 Elsevier Inc. All rights reserved.
doi:10.1016/j.jcat.2011.01.024

formed at the metal–support interface of the respective ceria-supported Pt or Au nanoparticles are responsible for catalyzing the low-temperature WGS reaction.

In the present work, the WGS reaction has been investigated over a series of ceria-supported Pt catalysts with the goal to understand the effect of Pt particle size on important kinetic and mechanistic aspects of the reaction. Toward this goal, steady-state isotopic transient kinetic analysis (SSITKA) coupled with DRIFTS and mass spectrometry experiments has been designed and performed to probe the chemical structure of *active* reaction intermediates and *spectator* species, and to estimate the surface concentration of *active* "H-containing" and "C-containing" intermediates found in the "hydrogen-path" and "carbon-path" of the reaction, respectively. The early seminal works by Tamaru [24], Matyshak [25], Happel [26], Goodwin [27], Chuang [28], Bennett [29] and their co-workers for the development of SSITKA and combined FTIR and SSITKA techniques should be acknowledged.

A novel transient isotopic experiment that allows quantifying the relative importance of the "redox" and "associative formate with –OH group regeneration" mechanisms in the present WGS reaction over Pt/CeO_2 has been designed, and results are presented in this work. The "redox" mechanism was also probed by the aid of an ^{18}O isotopic exchange-related experiment. Other *in situ* DRIFTS transient experiments were performed to follow the dynamic kinetics of the –COOH (formate) reaction during the CO/H_2O (WGS, steady state) → He (t) and CO/H_2O (WGS, steady state) → H_2O/He (t) gas switches with the goal to probe in a quantitative manner the decomposition of –COOH in He (inert gas) and in similar to WGS reaction conditions. I*n situ* DRIFTS-CO chemisorption/TPD studies have also been performed to better discuss the results obtained from the various ^{13}CO transient isotopic experiments.

2. Experimental

2.1. Catalyst preparation

The ceria-supported Pt catalysts were prepared by impregnating cerium dioxide (99.9%, Aldrich CAS 1306-38-3, powder <5 micron, BET = 5.6 m^2/g, and mean pore diameter, d_p = 10 nm) with an aqueous solution of $Pt(NH_3)_2(NO_2)_2$ (3.4 wt.% solution in NH_4OH, Aldrich). Ceria in powder form was first mixed under continuous stirring with de-ionized water (Milli-Q Direct 8), and a given amount of Pt precursor solution corresponding to the desired metal loading (0.1, 0.3, 0.6, 1.0 or 2.0 wt.% Pt) was then added. After gradual evaporation of water at 70 °C for 4 h, the resulting slurry was then dried at 120 °C overnight and placed in a furnace (ELF 11/6, Carbolite) for calcination to 600 °C in static air for 2 h using a heating rate of 50 °C/min. Prior to any catalytic measurements, the fresh catalyst sample was pre-treated with 20 vol.% O_2/He (50 N mL/min) gas mixture at 500 °C for 2 h followed by reduction in H_2 (1 bar, 50 N mL/min) at 300 °C for 2 h.

2.2. Catalyst characterization

2.2.1. H_2 temperature-programmed desorption (TPD) studies

The dispersion of Pt metal in the x wt.% Pt/CeO_2 catalysts was determined by selective H_2 chemisorption at 25 °C followed by temperature-programmed desorption (TPD) in He flow (30 N mL/min) using the apparatus and procedures described previously [30,31]. A 0.5-g fresh catalyst sample (Section 2.1) was first calcined in a 20 vol.% O_2/He gas mixture (50 N mL/min) at 500 °C for 2 h and then reduced in pure H_2 (30 N mL/min) at 300 °C for 2 h. Quantitative analysis of the effluent gas stream from the microreactor was done with *online* quadrupole mass spectrometer (Omnistar, Balzers) equipped with a fast response inlet capillary/leak valve (SVI050, Balzers) and data acquisition systems. The mass numbers (m/z) 2, 18, and 32 were continuously monitored for H_2, H_2O, and O_2, respectively. A H/Pt_s ratio of one for hydrogen chemisorption stoichiometry was assumed. The gaseous response of H_2 obtained by mass spectrometry was calibrated against a standard 0.1 vol.% H_2/He gas mixture. The accuracy of quantitative analysis of the signal response curves obtained from the H_2 chemisorption/TPD was within 5%. The accuracy of this procedure in determining Pt dispersions for Pt/CeO_2 catalysts was checked by HRTEM measurements which are described in what follows.

2.2.2. High-resolution transmission electron microscopy

Platinum particle size distribution and a mean Pt particle size for the x wt.% Pt/CeO_2 catalysts were estimated through high angle annular dark field (HAADF) images obtained using a 200-kV JEM-2100J (Jeol Ltd.) transmission electron microscope equipped with an INCAx-Sight (Oxford Inc.) energy-dispersive X-ray spectroscopy. HAADF images were recorded with the microscope in STEM mode with a beam size of 1 nm and an inner collection angle of 68.5 mrad. The contrast in HAADF images is mainly due to differences in the atomic number (Z) of metal elements at constant thickness. Given that Z_{Pt} = 78 and Z_{Ce} = 58, the brighter regions in the HAADF images correspond to Pt particles.

2.2.3. Temperature-programmed DRIFTS-CO chemisorption studies

A Perkin-Elmer Spectrum GX II FTIR spectrometer equipped with a high-temperature/high-pressure temperature controllable DRIFTS cell (Harrick, Praying Mantis) were used to record, in an *in situ* manner, infrared spectra obtained under reaction conditions. The spectrum of the solid taken in Ar flow at the desired reaction temperature, following catalyst pretreatment, was subtracted from the spectrum of the solid exposed to the reaction gas mixture. The catalyst pretreatment consisted of passing over the catalyst sample a 20 vol.% O_2/Ar gas mixture at 500 °C for 2 h followed by a switch to pure He gas and cooling the reactor to 300 °C. A gas switch to pure hydrogen for catalyst reduction at 300 °C for 2 h was then made. The following nomenclature is given for the above-described gas switches, and it is adopted in all other sequence of gas switches used in the present work: 20 vol.% O_2/Ar, 500 °C, 2 h → He, cool down to 300 °C → H_2 (1 bar), 300 °C, 2 h.

Signal averaging was set to 50 scans per spectrum, and the spectra were collected at the rate of 1 scan/s at a 2 cm^{-1} resolution in the 400–4000 cm^{-1} range. DRIFTS spectra when necessary were smoothed to remove high-frequency noise and further analyzed using the software Spectrum® for Windows in accordance with guidelines reported [32]. CO chemisorption was performed from a 2.98 vol.% CO/He gas mixture at 25 °C for 30 min. The gas flow was then switched to Ar, and the temperature of the solid was increased to 30, 70, 100, 150, 200, 300 and 400 °C in Ar flow, while DRIFTS spectra were recorded at each temperature. The DRIFTS flow-cell used in the present work was operated in the differential mode (30–35 mg of catalyst sample in fine powder form) without any significant channeling effects. This was proved by checking the CO conversion obtained in a typical WGS reaction experiment with respect to that obtained after using the same amount of catalyst and GHSV (h^{-1}) as in the plug-flow type micro-reactor used for kinetic and catalyst performance studies described in what follows.

2.3. Steady-state WGS kinetic reaction rate and catalyst performance measurements

Steady-state WGS kinetic reaction rate measurements were conducted in the experimental set-up previously described in detail [33] and using the Micro-reactivity Pro apparatus (ICP/CSIC, Spain). The initial kinetic rate of reaction at a given temperature was estimated from the slope of a X_{CO} versus W/F_{CO}° plot

constructed after varying the amount of catalyst, W (g) and keeping the GHSV (h^{-1}) constant (200 N mL/min, dilution of catalyst with SiO_2) and the CO conversion in the $0 < X_{CO} < 25\%$ range for the plug-flow type of the micro-reactor used [34]. Here, F_{CO}° is the feed molar flow rate (moles/s) of CO.

The performance of x wt.% Pt/CeO_2 catalysts in terms of X_{CO}(%) versus the reaction temperature in the 200–450 °C range was evaluated using an amount of catalyst, $W = 0.5$ g in powder form ($0.1 < d < 0.2$ mm) and a total volume flow rate, $F = 200$ N mL/min corresponding to a GHSV of about 40,000 ($L/L_{cat}/h$). After 1 h on reaction stream, where steady state in the reaction rate was achieved, the catalyst temperature was stepwise increased to the next temperature to be investigated. A stepwise decrease in reaction temperature showed that no deactivation of catalyst occurred during the 8-h period of catalytic measurements performed in the 200–450 °C range, as evidenced also by Pt dispersion measurements. The reaction feed composition used in all kinetic and catalyst performance studies consisted of 3 vol.% CO/10 vol.% H_2O/87 vol.% He. The effluent gas stream from the micro-reactor after removing the water (Peltier Gas Cooler, model ECP1000, M&C TechGroup) was directed to a mass spectrometer (Omnistar, Balzer) for *on line* monitoring of H_2, CO, and CO_2 gases. The purity of all gases (Linde Gas, Greece) used in the kinetic and catalyst performance experiments (e.g., H_2, He, CO, Ar) was higher than 99.95%.

External mass transport phenomena in the catalytic beds used for kinetic and catalyst performance evaluation tests were checked by varying the amount of catalyst and feed volume flow rate keeping the same GHSV (h^{-1}). For example, after using a catalyst bed of 0.5 g and a total flow rate of 200 N mL/min or 0.25 g and 100 N mL/min, similar CO conversions within 5% were estimated.

2.4. SSITKA-mass spectrometry studies

The isotopes used in the SSITKA experiments were ^{13}CO (99.9 atom% ^{13}C, Spectra Gases) and deuterium oxide (D_2O, 99.96 atom% D, Aldrich). SSITKA experiments were performed using two HPLC pumps (GILSON 307) for the addition of H_2O and D_2O to the reactor feed stream in the apparatus described elsewhere [33]. The SSITKA experiments performed in order to follow the "hydrogen-path" of reaction involved the switch 3 vol.% CO/10 vol.% H_2O/Ar/Kr (T, 30 min) → 3 vol.% CO/10 vol.% D_2O/Ar (T, t), while those to follow the "carbon-path" of reaction involved the switch 3 vol.% ^{12}CO/10 vol.% H_2O/Ar/He (T, 30 min) → 3 vol.% ^{13}CO/10 vol.% H_2O/Ar (T, t). The effluent wet gas stream of the reactor was passed through a condenser (Peltier system of low volume), the exit of which (dry gas) was directed to the mass spectrometer for *on line* recording of the normal and isotope-containing (D, ^{13}C) reactants and products (e.g., H_2, HD, D_2, ^{12}CO, ^{13}CO, $^{12}CO_2$, and $^{13}CO_2$) [33]. More details of the SSITKA experiments and the micro-reactor used were previously reported [35–37]. It was estimated that the response time, τ (s) of the system used in SSITKA studies (switching valve → micro-reactor → condenser → mass spectrometer) is about 5 s based on the transient response curve of Ar to the switch He → 1 vol.% Ar/He [35]. The mass of Pt/CeO_2 catalyst was adjusted in every SSITKA experiment so as to keep the CO conversion below 15%. The total mass of the catalyst bed was 0.5 g (catalyst + SiO_2 for dilution).

2.5. SSITKA-DRIFTS studies

SSITKA-DRIFTS experiments were performed in a specially designed gas flow-system where the response time of the DRIFTS reactor cell (~35 mg Pt/CeO_2) was about 5 s at a flow rate of 200 N mL/min [36]. Signal averaging was set to 50 scans per spectrum, and the spectra were collected in the 4000–500 cm^{-1} range at the rate of 0.2 scans/s (MCT detector) and at a resolution of 2 cm^{-1}. The background spectrum of the solid catalyst was taken under 10 vol.% H_2O/Ar flow at the desired reaction temperature. The DRIFTS data are reported as log (1/R) (absorbance mode) using the relationship, $R = I/I_0$. Here, R is the catalyst sample reflectance, I_0 is the absorbance intensity of the solid itself, and I is the absorbance intensity of both the solid catalyst and the adsorbed species under reaction conditions. The function log (1/R) was found to give a better linear correlation of the integral band against surface coverage than that given by the Kubelka–Munk function for strongly absorbing media [38]. SSITKA-DRIFTS experiments with ^{13}CO (99.9 atom% ^{13}C, Spectra Gases) involved the switch 3 vol.% ^{12}CO/10 vol.% H_2O/Ar/He (T, 30 min) → 3 vol.% ^{13}CO/10 vol.% H_2O/Ar (T, t) at a total flow rate of 200 N mL/min which potentially allows determining the chemical structure of the *active* intermediate and spectator species of the WGS reaction.

2.6. In situ DRIFTS combined with kinetic analyses studies

In order to gather further experimental evidence whether linear adsorbed CO and –COOH could be considered truly active adsorbed reaction intermediates, additional transient experiments were performed using the DRIFTS reactor cell. These included the following gas switches (step change mode):

(a) 3 vol.% CO/10 vol.% H_2O/He (T, 30 min) → *He (300 °C, t)*, and
(b) 3 vol.% CO/10 vol.% H_2O/Ar/He (300 °C, 30 min) → *10 vol.% H_2O/He (300 °C, t)*.

The aim was to describe the dynamic kinetics of desorption and reaction of adsorbed CO and –COOH, the latter formed during the WGS reaction, under the He and H_2O/He gas atmospheres. The rate constant (k, s^{-1}) associated with –COOH reaction toward CO_2 and H_2 under H_2O/He flow (reflecting the WGS reaction, expt. (b)) is compared to that of –COOH reaction (decomposition) in He flow (expt. (a)).

2.7. ^{13}CO transient isothermal isotopic exchange performed after WGS followed by H_2O reaction

A novel experiment was designed and performed which allowed the measurement of the initial rate of reaction of adsorbed formate and CO with water alone, where the surface concentrations of the former species were established under steady-state WGS reaction conditions. The experiment was as follows: after a steady-state WGS reaction rate was reached on the catalyst surface, the 3 vol.% ^{12}CO/10 vol.% H_2O/Ar feed stream was changed (step change) to a 3 vol.% ^{13}CO/Ar gas mixture for 3 min in order to replace adsorbed ^{12}CO with ^{13}CO and leave on the catalyst surface the non-exchangeable $^{12}COOH$ (formate) species formed under the WGS ($^{12}CO/H_2O$/Ar) reaction conditions. The feed was subsequently changed to a 10 vol.% H_2O/Ar gas, and at the same time, the transient responses of $^{12}CO_2$, $^{13}CO_2$ and H_2 were continuously monitored by *online* mass spectrometer (Section 2.4). The initial transient rates of $^{12}CO_2$ and $^{13}CO_2$ formation are considered as characteristic rates of the reaction of water with adsorbed $^{12}COOH$-s and ^{13}CO-s intermediates, and allow discriminating the prevailing mechanism, e.g., "redox" versus "associative formate". The shape of the $^{12}CO_2$ and $^{13}CO_2$ isotopic response curves obtained reflects the kinetics of reaction of adsorbed formate and CO with water.

2.8. $^{18}O/^{16}O$ isotope exchange followed by WGS reaction

$^{18}O/^{16}O$ isotopic exchange experiments were carried out in the same apparatus used for SSITKA-mass spectrometry studies (Section 2.4). The catalyst sample (0.3 g) was first pre-treated with

5 vol.% $^{18}O_2$/He (97% ^{18}O, Marshall isotopes Ltd.) at 600 °C for 30 min, purged with He and cooled to 80 °C. The feed was then switched to H_2 (1 bar) at 80 °C for 20 min to reduce only PtO_x to Pt^o. Following this gas treatment, the catalyst was then heated from 80 to 300 °C in Ar flow and then exposed to the WGS reaction feed stream (3 vol.% CO/10 vol.% H_2O/Ar; 200 N mL/min). The $^{18}O/^{16}O$ isotopic exchange was monitored with mass spectrometry by recording the evolution of $^{16}O_2$, $^{16}O^{18}O$ and $^{18}O_2$ gaseous species (m/z = 32, 34 and 36), while mass numbers (m/z) 2 (H_2), 28 ($C^{16}O$), 44 ($C^{16}O_2$), 46 ($C^{16}O^{18}O$) and 48 ($C^{18}O_2$) were continuously monitored under the WGS reaction conditions.

3. Results and discussion

3.1. H_2 temperature-programmed desorption (H_2-TPD) studies

Hydrogen temperature-programmed desorption (H_2-TPD) studies were conducted in order to investigate the effect of Pt particle size on the interaction of H_2 with the ceria-supported Pt surface (adsorption states, binding energy, E_{Pt-H}), where the dispersion (D, %) and the mean particle size ($\bar{d}_{Pt}$) of Pt metal can also be estimated, and the obtained values were compared with those directly obtained from HRTEM (see Section 3.2). Fig. 1 shows H_2-TPD response curves obtained over the fresh 0.6 wt.% Pt/CeO_2 (Fig. 1a) and 2.0 wt.% Pt/CeO_2 (Fig. 1b) catalysts. The amount of H_2 desorbed, N_H (μmol H/g), the dispersion, D (%), the mean Pt particle size, $\bar{d}_{Pt}$ (nm), and the observed peak temperature maxima, T_M (°C) for all five ceria-supported Pt catalysts investigated are provided in Table 1. It is noted that the dispersion of Pt was based on the total amount of hydrogen desorbed, N_H, and that no H_2 adsorption was evidenced after performing a similar H_2 chemisorption/TPD experiment on CeO_2 alone.

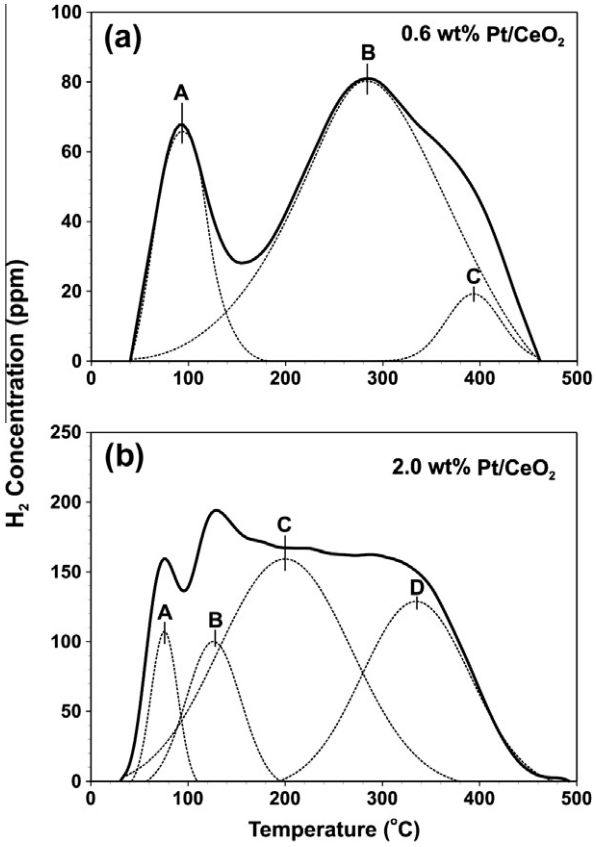

Fig. 1. H_2-TPD response curves obtained over (a) 0.6 wt.% Pt/CeO_2 and (b) 2.0 wt.% Pt/CeO_2 catalysts after H_2 chemisorption at 25 °C. The deconvolution of TPD response curves is also shown. Experimental conditions: W = 0.5 g, β = 30 °C/min, Q_{He} = 30 N mL/min.

In the case of 0.6 wt.% Pt/CeO_2 catalyst (Fig. 1a), two well-defined desorption peaks are apparent with maxima at 93 (peak A) and 286 °C (peak B), respectively, and a shoulder at the falling part of peak B. After deconvolution and curve fitting procedures (Gaussian peak shapes), the shoulder is due to a third hydrogen adsorption state (Fig. 1a, peak C, T_M = 395 °C). Peak A is assigned to a weakly adsorbed atomic hydrogen state on Pt, whereas peaks B and C to strongly adsorbed states on Pt [39–41]. As it will be shown in the following section, the H_2 chemisorption/TPD methodology provided hydrogen dispersions (H/Pt_s) and corresponding mean Pt particle sizes similar within 10–20% to those estimated by HRTEM direct measurements. Even though the amount of N_H estimated (Table 1) provides values of H/Pt lower than one, which suggests that hydrogen spillover may not be of concern, the latter phenomenon might be considered to take place only to a small extent given the good agreement between the H_2 chemisorption and HRTEM results.

In the case of 2.0 wt.% Pt/CeO_2 catalyst (Fig. 1b), a largely different H_2-TPD profile is observed, where four hydrogen desorption peaks were identified. The low-temperature peak (peak A, T_M = 71 °C) corresponds to a weakly bound atomic hydrogen (H) state on Pt, while peaks B, C, and D (T_M = 121, 196, and 336 °C, respectively) to irreversibly adsorbed H states of higher binding strength, E_{Pt-H}.

The HRTEM measurements performed on the present 0.6 and 2.0 wt.% Pt/CeO_2 catalysts (Section 3.2) revealed a rather wide Pt particle size distribution. This result should be related to the various hydrogen adsorption states observed in the H_2-TPDs (Fig. 1). Collins and Spicer [42] have reported H_2-TPD spectra on polycrystalline Pt, where desorption of hydrogen below 130 °C was attributed to adsorption on the terraces, whereas desorption above 130 °C to adsorption at steps. Given the rather wide Pt particle size distribution seen in the present Pt/CeO_2 catalysts, and the fact that the distribution of Pt sites of different coordination number depends on the Pt particle size [43,44], the observed adsorption states of atomic hydrogen in the H_2-TPDs (Fig. 1) are in line with these observations. On the other hand, hydrogen adsorbed on Pt sites located at the Pt–CeO_2 interface may not be excluded [40].

Bernal et al. [39] reported H_2-TPD traces on a 2.5 wt.% Pt/CeO_2 catalyst after reduction of the latter in hydrogen at 500 °C. The obtained hydrogen desorption profile is in very good agreement with the present one reported in Fig. 1b, given the different heating rate and carrier gas flow rate used (ca. 10 °C/min, 60 N mL/min) compared to the ones used in the present work, and the expected effect of these experimental parameters on the position and features of TPD response [45,46]. It is also interesting to note that Zafiris and Gorte [41] reported multiple hydrogen adsorption states on

Table 1
Amount of H_2 desorbed (μmol H g^{-1}), dispersion of Pt (D, %), and Pt mean particle size ($\bar{d}_{Pt}$, nm) estimated from H_2-TPD experiments on x wt.% Pt/CeO_2 (x = 0.1–2.0) catalysts. The peak maximum desorption temperatures (T_M) determined after deconvolution and curve fitting of H_2-TPD curves are also given.

Pt loading (wt.%)	N_H (μmol H g^{-1})	D (%)	$\bar{d}_{Pt}$ (nm)[a]	T_M^1 (°C)	T_M^2 (°C)	T_M^3 (°C)
0.1	4.3	84	1.3	98	222	336
0.3	9.5	61	1.8	115	289	378
0.6	11.3	37	3.0[b]	93	286	395
1.0	10.0	22	5.0[b]	120	205	307
2.0	13.8	13.7	8.0[b]	71	121, 196	336

[a] Use of the formula: $\bar{d}_{Pt}$ (nm) = 1.1/D.
[b] The obtained values agree within 10–20% of the values determined from STEM studies (mean Pt particle size based on the measured particle size distribution).

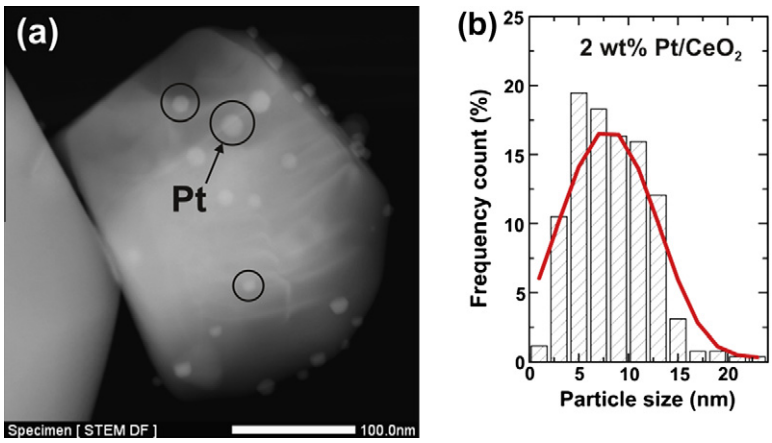

Fig. 2. STEM image (a) and Pt particle size distribution (b) obtained over a 2.0 wt.% Pt/CeO_2 catalyst sample calcined at 500 °C in 20 vol.% O_2/He and reduced in H_2 at 300 °C.

a 10-nm Pt particle supported on amorphous ceria film as opposed to the case of 3-nm Pt size, in harmony with the present H_2-TPDs of Fig. 1.

It was reported [45,46] that readsorption effects in supported metal catalysts during TPD are important and can influence significantly the appearance of peak maximum desorption temperature, T_M, for a 2nd order desorption kinetics (e.g., H_2-TPD) but do not result in the formation of large shoulders or multiple peaks. Therefore, the assignment of the deconvoluted TPD trace shown in Fig. 1 into multiple states of hydrogen adsorption on Pt is reasonable.

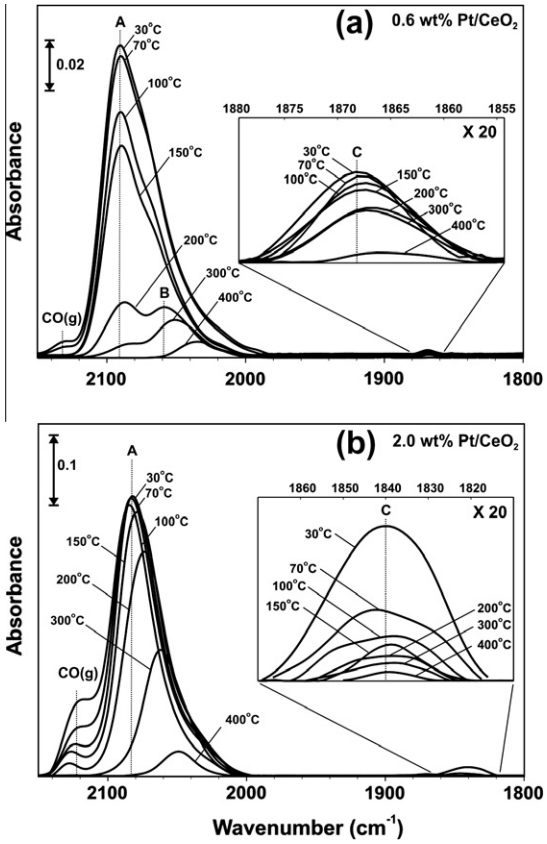

Fig. 3. *In situ* DRIFTS spectra recorded in the 2150–1800 cm^{-1} range after CO chemisorption at 25 °C and TPD (up to 400 °C in Ar flow) over (a) 0.6 wt.% Pt/CeO_2 and (b) 2.0 wt.% Pt/CeO_2 catalysts.

3.2. HRTEM studies

Fig. 2a shows high angle annular dark field (HAADF) images (STEM mode) obtained on the fresh (after calcination at 500 °C and H_2 reduction at 300 °C) 2 wt.% Pt/CeO_2 catalyst. It is clearly seen that practically hemispherical Pt particles are obtained which were deposited on very crystalline CeO_2 particles (50–400 nm). Fig. 2b shows the corresponding Pt particle size distribution obtained after counting about 300 particles, where a mean Pt particle size of 8.4 (±3.8 nm) was estimated. Similar rather broad Pt particle size distributions were obtained for the 0.6 and 1.0 wt.% Pt/CeO_2 catalysts. Based on EDS analyses in the region on top of Pt particles, no decoration effects of Pt by reducible CeO_x species were seen in agreement with HRTEM images reported elsewhere [39] for hydrogen reduction temperatures below 500 °C.

The results obtained from the STEM studies (Fig. 2) in terms of the mean Pt particle size agree very well with the H_2 chemisorption/TPD result reported and discussed previously (Fig. 1b). As reported in Table 1, a mean Pt particle size of 8.0 nm was estimated assuming spherical geometry, as proved to be the case by the STEM studies (Fig. 2a). Overall, the STEM studies provided a Pt mean particle size within 10–20% of that estimated by the H_2 chemisorption/TPD technique (Fig. 1).

3.3. DRIFTS studies on the interaction of CO with Pt/CeO_2 catalysts

Fig. 3 presents DRIFTS-CO/TPD spectra recorded in the 2150–1800 cm^{-1} range under Ar flow at various temperatures (30–400 °C) following CO chemisorption (25 °C, 30 min) over the 0.6 wt.% Pt/CeO_2 (Fig. 3a) and 2.0 wt.% Pt/CeO_2 (Fig. 3b) catalysts. Similar spectra to those reported in Fig. 3a were recorded on the 0.1 wt.% Pt/CeO_2 catalyst, where no important differences had been observed. As shown in Fig. 3a, at desorption temperatures below 150 °C a well-defined infrared band (peak A) and a shoulder (peak B) in the 2120–1980 cm^{-1} range were identified, the latter emerging as a clear IR band at desorption temperatures larger than 150 °C. These two IR bands correspond to high-frequency (HF) and low-frequency (LF) linear adsorbed CO on Pt reflecting a distribution in CO adsorption sites on the Pt surface, in harmony with the broad Pt particle size distribution observed (see Section 3.2). For the largest Pt mean particle size of 8.0 nm (2.0 wt.% Pt/CeO_2), only the HF-linear adsorbed CO is observed (peak A, Fig. 3b). The presence of adsorbed bridged CO on Pt also appeared in the 1880–1810 cm^{-1} range (peak C, inset spectrum, Fig. 3a and b). As will be shown later on in Section 3.5.2, the LF-linear adsorbed CO was the only species populated under WGS reaction at 300 °C.

The assignment of the various kinds of adsorbed CO was based on well-documented literature data [47–57].

The stepwise increase in desorption temperature from 25 to 400 °C in Ar flow which resulted in the progressive decrease in the integral and infrared band intensity associated with linear CO (peaks A and B) and bridge-bonded CO on Pt (peak C, Fig. 3) is in harmony with the CO-TPDs (see Appendix A: Supplementary material), where dissociation and oxidation reactions of adsorbed CO on Pt took place up to 300 °C, resulting in two CO_2 desorption peaks. Fig. 3a indicates that the HF-linear adsorbed CO (peak A) disappears above 300 °C, whereas the LF-linear CO appears more thermally stable and disappears above 400 °C. The absence of a LF-linear CO in Fig. 3b reflects stronger C–O bond, consistent with a weaker Pt–CO bond over the 2.0 wt.% Pt/CeO_2 compared with 0.6 wt.% Pt/CeO_2 catalyst. This result strongly suggests the influence of Pt particle size on the chemisorptive properties of CO, as evidenced also by the CO-TPD and H_2-TPD profiles (Fig. 1) obtained. These remarks are in good agreement with the early work by Zafiris and Gorte [41] who found that the high-temperature desorption state of CO was larger in population on the smaller than the larger Pt crystallites, in harmony with the concept that small metal particles have a larger percentage of lower coordination Pt atoms than large metal particles.

The progressive decrease in the IR intensity of integral band (Fig. 3a) is accompanied by a red shift of the 2068 cm^{-1} (LF-linear CO) and 1869 cm^{-1} (bridged CO) IR bands to 2032 cm^{-1} and 1863 cm^{-1}, respectively, which is consistent with a decrease in dipole–dipole coupling between adsorbed CO species due to the decrease in surface coverage [53,58]. A similar effect was also observed in the case of 2.0 wt.% Pt/CeO_2 catalyst (Fig. 3b). It was shown [58] that chemisorption of an electron donor compound on Pt results also in a substantial decrease in the ν(CO) frequency due to an electron transfer toward platinum, the result of which is an increase in back-donation of metal electron density into the $2\pi^*$ antibonding orbital of adsorbed CO. Such an electron donor species for the present case could be considered that of "carbon" formed by CO disproportionation during TPD. As pointed out by Collins and Spicer [42], a build-up of carbon by disproportionation of CO on bare Pt surfaces occurs to a very limited extent.

3.4. Catalytic activity and kinetic rate measurements on Pt/CeO_2 – effect of Pt particle size

3.4.1. Catalytic activity performance studies

The effect of Pt loading (x wt.%) or equivalently of Pt mean particle size (d_{Pt}, nm) and dispersion (D, %) on the catalytic performance in terms of CO conversion of Pt/CeO_2 solids toward the WGS reaction is presented in Fig. 4. The conversion of carbon monoxide is given by:

$$X_{CO}(\%) = (F_{CO}^{in} - F_{CO}^{out})/F_{CO}^{in} \times 100 \quad (1)$$

where F_{CO}^{in} and F_{CO}^{out} are the molar flow rates (moles/min) of CO at the reactor inlet and outlet, respectively. The CO conversion versus temperature profile at thermodynamic equilibrium conditions is also given (X_{eq}, Fig. 4). This curve was derived using the temperature-dependent equilibrium constant relationship and appropriate mass balances [37]. This curve shows that below 200 °C full CO conversion is achieved, whereas a decrease in CO conversion by 6.5% units is noticed at 450 °C.

It is observed that ceria alone is practically inactive in the 200–400 °C range (Fig. 4). Addition of a small amount of Pt (e.g., 0.1 wt.%) on ceria results in a significant increase in WGS activity. A progressive shift in the CO conversion vs. temperature profile toward lower reaction temperatures is clearly observed by increasing

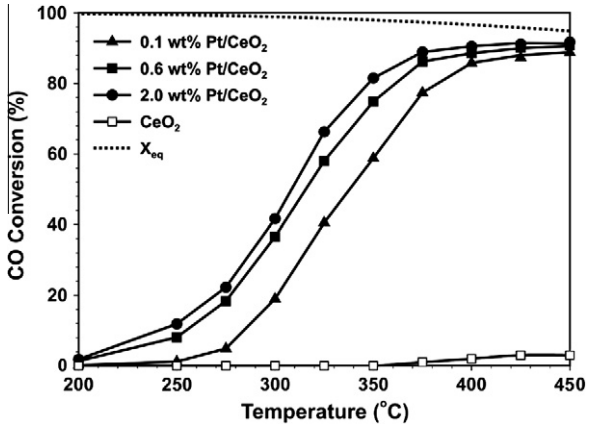

Fig. 4. Effect of platinum loading (0–2.0 wt.% Pt) on the conversion of CO as a function of WGS reaction temperature obtained over ceria-supported Pt catalysts. The CO conversion (X_{eq}) versus temperature profile for equilibrium conditions ($y_{CO}^{f} = 0.03$ and $y_{H_2O}^{f} = 0.1$) is also shown. Experiments were performed with constant $W/F = 0.0025$ g min/cm^3.

Pt loading in the 0.1–2.0 wt.% range (Fig. 4). For example, a CO conversion value of 45% is obtained at 300 °C using 2.0 wt.% Pt compared to 325 °C after using 0.1 wt.% Pt. On the other hand, at 300 °C the CO conversion is increased by a factor of 2.2 after increasing the Pt loading from 0.1 to 2.0 wt.%. As will be illustrated below, the progressive increase in CO conversion or the equivalent integral reaction rate with increasing Pt loading can be understood by the progressive increase in the specific kinetic reaction rate per length of perimeter of the Pt–CeO_2 interface (μmol CO cm^{-1} s^{-1}) with increasing Pt loading or equivalently of Pt particle size (Table 1). Similar results to those of Fig. 4 were obtained by Jacobs et al. [18] who concluded that higher Pt loadings enhance partial reduction of ceria at low temperatures (H_2-TPR studies), and as a result of this higher active site densities of bridging OH groups associated with Ce^{3+} are obtained. It should be noted that at 450 °C (Fig. 4), the experimentally obtained CO conversion deviates by about 5% from the corresponding equilibrium value, a result which is within the experimental error of measurements.

3.4.2. Kinetic rate measurements of WGS reaction

Fig. 5 presents linear plots of X_{CO} (fractional conversion) versus the quantity W/F_{CO}^{o} (g s μmol^{-1}) at 275 °C for two ceria-supported Pt catalysts (0.6 and 2.0 wt.% Pt), where the initial kinetic rate can be obtained directly from the slope of this linear relationship for

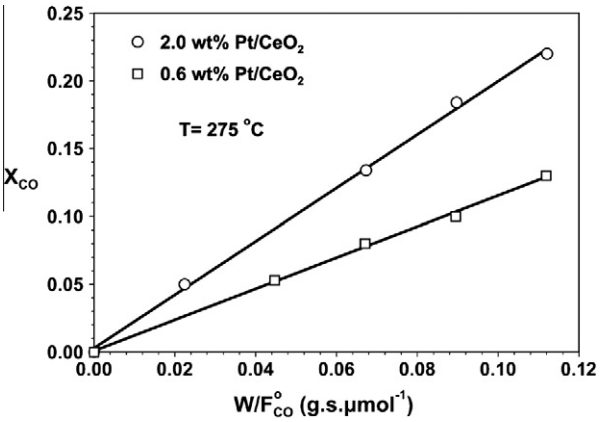

Fig. 5. Plots of CO conversion (X_{CO}) versus W/F_{CO}^{o} for the estimation of kinetic initial rate of WGS reaction at 275 °C over the 0.6 and 2.0 wt.% Pt/CeO_2 catalysts.

the plug-flow type of micro-reactor used [34]. Similar linear plots ($0.97 < R^2 < 0.99$) were obtained for the other ceria-supported Pt catalysts and reaction temperatures of 250 and 300 °C investigated.

In order to check whether external mass transport resistances were present under the conditions of the kinetic reaction rate measurements performed (Fig. 5), two sets of W(g) and F (NmL/min) experimental parameters were used keeping their ratio constant. It was found that at 300 °C and for the 1.0 wt.% Pt/CeO_2 catalyst, the X_{CO} was 39% and 41%, respectively, after using the W/F = 0.5 g/200 N mL/min and 0.25 g/100 N mL/min values. This result proves that up to 300 °C, external mass transfer was practically absent for the kinetic studies performed. The absence of internal mass and heat transport resistances within the catalyst particle's pore system was also checked and results are provided in Appendix A: Supplementary material section. It was found that all kinetic rate measurements were not influenced by internal mass and heat transport resistances. Negligible temperature difference was also estimated between the measured gas phase temperature and that at the surface of the catalyst particle.

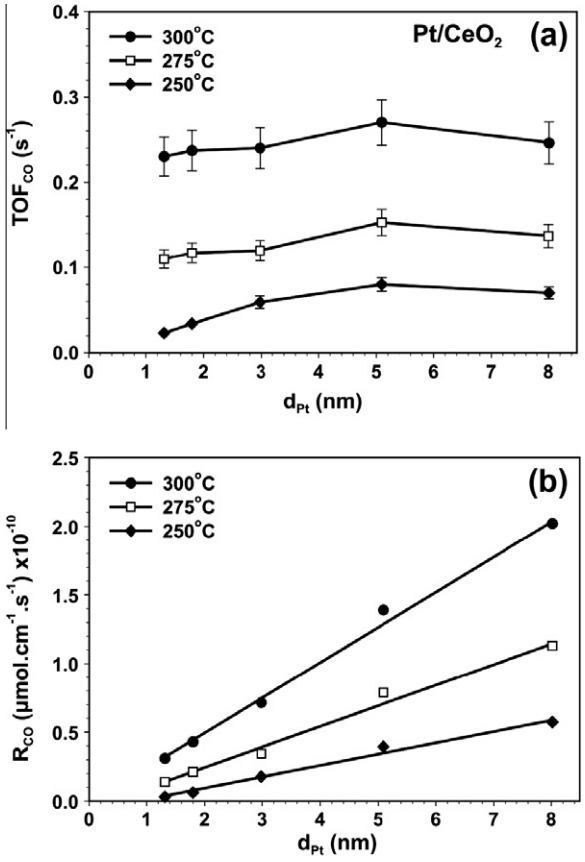

Fig. 6. Effect of mean Pt particle size (d_{Pt}) on the specific kinetic rate of WGS reaction in terms of turnover frequency (TOF_{CO}, s^{-1}) based on the Pt exposed surface atoms (a), and on the length of perimeter of Pt–ceria interface (cm/g), R_{CO} (μmol cm^{-1} s^{-1}) (b) at 250, 275, and 300 °C.

Fig. 6a and b presents the dependence of intrinsic kinetic rate (Fig. 5) of the WGS reaction at T = 250, 275, and 300 °C on the mean Pt particle size, when the kinetic rate is based on the Pt exposed surface area, TOF (s^{-1}), and on the length of the perimeter of the Pt–ceria interface (μmols cm^{-1} s^{-1}), respectively. For each Pt/CeO_2 catalyst, the length of the perimeter of Pt–ceria interface, I_0 (cm/g) was estimated considering that for each Pt nanoparticle (Fig. 2a) a circular geometry for the interface applies, and accounting for the Pt loading and the corresponding mean particle size (Table 1), and using a Pt density, ρ = 21.3 g/cm^3. Values of I_0 for three of the present Pt/CeO_2 catalysts are reported in Table 2. It is clearly observed that the TOF (s^{-1}) is rather insensitive to the Pt particle size. More precisely, differences in TOF of less than 20% were estimated at T = 275 and 300 °C, and only an increase of TOF by a factor of 2 was obtained in the case of 1.3 and 8.0 nm Pt particle size at the lowest temperature of 250 °C. These results are in very good agreement with results reported on the same Pt/CeO_2 catalytic system (2.0–9.0 nm Pt) for the WGS reaction (see Fig. 3, Ref. [59]). The authors [59] have also reported that the activity of Pt/CeO_2 was not dependent on the structural and morphological characteristics of ceria support. Based on the TOF results obtained in the 225–300 °C range, an apparent activation energy, E_{app}, in the 14.5–16.5 (±1) kcal mol^{-1} range was estimated for Pt particle sizes in the 1.3–8.0 nm range. This result is in harmony with the works by Panagiotopoulou et al. [59,60] who used a similar ceria support (E_{app} = 18 kcal mol^{-1}).

In the case where the specific kinetic rate is estimated based on the periphery of Pt–CeO_2 interface, I_0 (cm/g), a linear correlation with the Pt particle size is obtained (Fig. 6b). Considering the fact that the number density (atoms/cm) of oxygen sites along the periphery of a Pt nanoparticle is dependent of Pt particle size, then obviously the same linear correlation as that shown in Fig. 6b will be obtained for the specific rate expressed per site located at the periphery of Pt–CeO_2 interface. Therefore, the differences by a factor of 3.3 in the specific reaction rates obtained at 300 °C (Fig. 6b) between the 1.3 and 8.0-nm Pt particle sizes cannot be accounted for exclusively by their difference in I_0 (cm/g) (see Table 2). It is therefore suggested that active sites along the Pt–ceria interface should possess different intrinsic site reactivity depending on the Pt particle size. As will be discussed next, the chemical structure of such sites is Pt–O–Ce and Ce^{3+}–□–Ce^{3+}. Thus, it is conceivable that as the Pt particle size decreases, the presence of Pt atoms with lower coordination, and thus local electron density, will be different. Given the fact that electron transfer between adjacent oxygen (support) and Pt atoms is expected [61], the reactivity of oxygen atoms of support will then be influenced by the size of the Pt nanoparticles. It is important to note that the small difference by 1–2 kcal/mol obtained in the E_{app} of the reaction between the small (1.3 nm) and large (8.0 nm) Pt particle sizes results in an increase

Table 2
Amount (μmol g^{-1}), number density (atoms $g^{-1} \times 10^{18}$), and surface coverage (θ) of active "hydrogen-containing" (H-pool) and "carbon-containing" (C-pool) species found in the mechanism of the WGS reaction at 300 °C over x wt.% Pt/CeO_2 catalysts (x = 0.1, 0.6, and 2.0) measured by SSITKA-mass spectrometry. The estimated total length of Pt–CeO_2 interface (cm/g_{cat}) and active oxygen site density (atoms $g^{-1} \times 10^{18}$) along the periphery of hemispherical Pt crystallites are also given.

Pt loading (wt.%)	H-pool (μmol g^{-1}) or (atoms g^{-1}) × 10^{18}	C-pool (μmol g^{-1}) or (atoms g^{-1}) × 10^{18}	Total specific length of Pt–CeO_2 interface, I_0 (cm/g)	Estimated active oxygen sites density in I_0 (atoms g^{-1}) × 10^{18}
0.1	2.6/1.6 (0.6)[a]	0.7/0.4(0.15)[b]	3.2×10^{10}	0.85
0.6	8.6/5.2 (0.75)[a]	1.9/1.1 (0.17)[b]	3.8×10^{10}	1.0
2.0	3.5/2.1 (0.25)[a]	0.5/0.3 (0.03)[b]	1.7×10^{10}	0.44

[a] Number in parenthesis represents the amount of "H-pool" in equivalent monolayers (θ) based on the Pt surface area.
[b] Number in parenthesis represents the amount of "C-pool" in equivalent monolayers (θ) based on the Pt surface area.

of the exponential factor associated with k_{app} at 300 °C by a factor between 2.4 and 5.8, the result that could explain satisfactorily the observed specific kinetic rates shown in Fig. 6b. Furthermore, the number density of the active sites previously mentioned is expected to be controlled by the extent of charge transfer between Pt and O atoms within a narrow zone around the periphery of Pt–ceria interface, parameter that could also be used to explain the kinetic results shown in Fig. 6b.

A recent work on CO oxidation [62] on CuO/CeO_2 catalytic systems presented linear relationships between TOF (s^{-1}) and particle size of supported CuO on CeO_2, where the TOF was estimated based on the site density on the periphery of the $CuO–CeO_2$ interface, which is proved to be proportional to the size of the supported CuO crystallites. Thus, the authors concluded that a simple explanation for the linear relationship obtained between TOF_{CO} (s^{-1}) and d_{CuO} (nm) was the higher CO adsorption density on a larger CuO crystallite. This explanation implies also that the chemical step of chemisorbed CO reacting with active oxygen of ceria support is a rate-determining step.

3.5. Mechanistic aspects of the WGS reaction on Pt/CeO_2

3.5.1. SSITKA-mass spectrometry

Fig. 7a presents transient concentration response curves of H_2, HD, D_2, and Kr obtained after the isotopic switch 3 vol.% CO/10 vol.% H_2O/Ar/Kr (300 °C, 30 min) → 3 vol.% CO/10 vol.% D_2O/Ar (300 °C, t) was made over the 0.1 wt.% Pt/CeO_2 catalyst. The concentration (μmol g^{-1}) of *active* "H-containing" reaction intermediates, named "H-pool", is estimated based on the transient response curves of H_2, HD and Kr as described in Appendix A: Supplementary material section and previously reported [36,37], and the obtained results are given in Table 2 for the 0.1, 0.6, and 2.0 wt.% Pt/CeO_2 catalysts. The equivalent amount of "H-pool" in terms of surface Pt monolayers (θ) is also provided in Table 2 (numbers in parentheses).

Fig. 7b presents similar dimensionless gas phase transient concentration (Z) response curves for $^{12}CO_2$, $^{13}CO_2$, and He obtained after the isotopic switch 3 vol.% ^{12}CO/10 vol.% H_2O/Ar/He (300 °C, 30 min) → 3 vol.% ^{13}CO/10 vol.% H_2O/Ar (300 °C, t) was made. The concentration of *active* "carbon-containing" reaction intermediates, named "C-pool" which are found in the "carbon-path" of the WGS reaction was estimated based on the $^{12}CO_2$ and He response curves as described in Appendix A: Supplementary material section and previously reported [37], and results are given in Table 2. No ^{13}C-isotopic kinetic effect was observed since the steady-state rates of $^{12}CO_2$ and $^{13}CO_2$ under the non-isotopic and isotopic CO/H_2O gas mixtures were the same. The position of the $^{12}CO_2(g)$ and $^{13}CO_2(g)$ transient response curves in time under the $^{13}CO/H_2O$ switch must be such that the sum of the concentrations of $^{12}CO_2$ and $^{13}CO_2$ are equal to the steady-state concentration value of $^{12}CO_2$ obtained under the $^{12}CO/H_2O$ gas treatment. This means that in terms of the dimensionless concentration Z (Fig. 7b), the sum of $Z(^{12}CO_2)$ and $Z(^{13}CO_2)$ must be equal to 1.0 at any time during the transient. The latter important criterion of the SSITKA experiment was fully satisfied (Fig. 7b). In fact, the two transient response curves cross each other at $Z = 0.49$ instead of 0.5 (~2% experimental error).

In an effort to check whether the concentration (μmol g^{-1}) of active "hydrogen-containing" reaction intermediates estimated from the SSITKA-mass spectrometry experiments (Fig. 7a, Table 2) can be justified as formed along the metal–support interface, the number density (atoms g^{-1}) of oxygen sites along the periphery of $Pt–CeO_2$ interface was estimated and reported in Table 2, last column. In these calculations, a distance of 3.8 Å between two adjacent oxygen atoms of ceria support [63] each one accommodating a reaction intermediate species, as will be discussed next, was considered. The chemical nature of likely active "hydrogen-containing" intermediates is considered to be that of labile hydroxyl groups, –OH, and/or H species attached on surface O^{n-} of ceria support and/or adsorbed on the Pt surface, and formate species, –COOH. The latter was identified by SSITKA-DRIFTS and other experiments to be presented and discussed in the next section. According to Jacobs et al. [18–20,64–68], the active –OH groups are classified as type-II bridging, geminal, or terminal –OH groups formed on partially reduced ceria. They proposed that their formation arises either from hydrogen dissociation on the metal followed by spillover of the thus formed H species to the ceria support surface to generate bridging –OH groups, accompanied by a change in the oxidation state of Ce (Ce^{4+} to Ce^{3+}), or removal of surface capping oxygen atoms of ceria by H_2 or CO to generate oxygen vacancies (Ce^{3+} sites). On the latter sites, H_2O dissociation occurs, resulting in the formation of bridging –OH groups active in the WGS reaction [9,11–13,64,67,69,70].

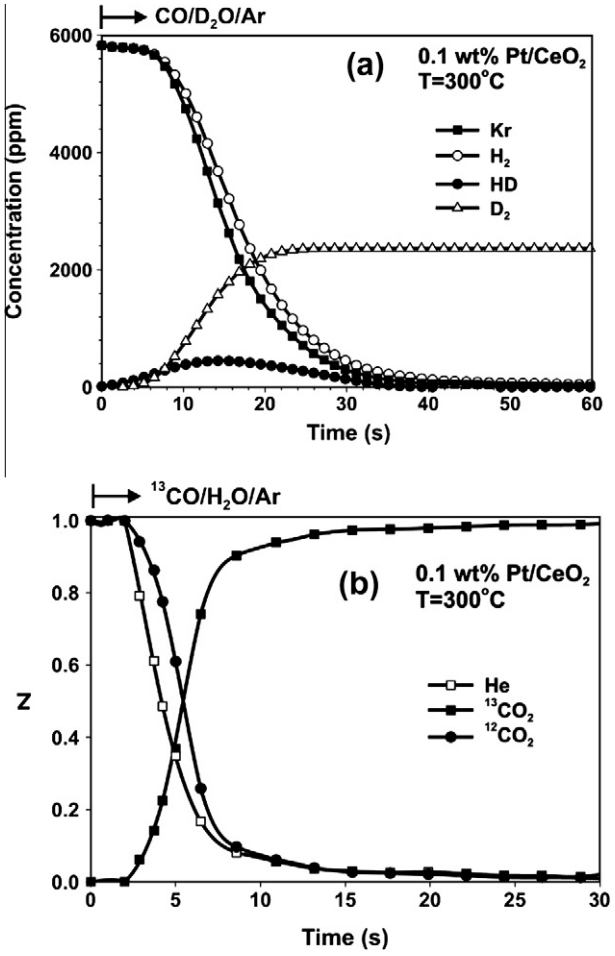

Fig. 7. SSITKA-mass spectrometry experiments performed in order to estimate the *active* (a) "hydrogen-containing" (H-pool) and (b) "carbon-containing" (C-pool) reaction intermediates found in the WGS reaction path on 0.1 wt.% Pt/CeO_2 catalyst at 300 °C. Gas delivery sequence: (a) 3 vol.% CO/10 vol.% H_2O/Ar/Kr (30 min) → 3 vol.% CO/10 vol.% D_2O/Ar (t) and (b) 3 vol.% ^{12}CO/10 vol.% H_2O/Ar/He (30 min) → 3 vol.% ^{13}CO/10 vol.% H_2O/Ar (t).

As seen in Table 2, the experimentally measured concentration of "C-pool" (atoms g^{-1}) in the 0.6 and 2.0 wt.% Pt/CeO_2 catalysts is similar to the theoretically estimated one, while it is half of that for the 0.1 wt.% Pt/CeO_2 catalyst. As will be discussed in the next section, the "C-pool" comprises of adsorbed formate (–COOH) and CO species, both associated with chemical bonding with a support

oxygen, and the CO-adsorbed species with a Pt surface atom as well (see Section 3.7). Therefore, it can be concluded that it is justifiable to consider that active formate species reside along the periphery of Pt–ceria interface and on sites next to it.

Regarding now the size of the "H-pool" (atoms g^{-1}) on the 0.1 wt.% Pt/CeO_2 catalyst, it is twice the theoretically estimated number of sites, while in the case of 0.6 and 2.0 wt.% Pt/CeO_2 catalysts, the experimentally measured concentration of "H-pool" is 5.2 and 4.8 times larger, respectively, than the theoretically estimated values (Table 2). This important result implies that the active OH/H species participating in the "hydrogen-path" of the WGS reaction reside within a zone from the Pt–ceria interface. This important conclusion finds support from previous observations made on the $Pt/\gamma\text{-}Al_2O_3$ [36,37], Au/CeO_2 [71,72], and Pt/CeO_2 [73] catalysts for the presence of a reactive and a non-reactive zone around the metal particle under steady-state WGS reaction conditions, where active species (e.g., –OH and –COOH) must diffuse toward the metal–support interface, where metal sites are required for the formation of reaction products (e.g., formate decomposition, di-hydrogen formation). It is interesting to note that a large increase in "H-pool" and "C-pool" occurs when increasing the Pt loading from 0.1 to 0.6 wt.%, whereas a corresponding large decrease occurs by further increasing Pt loading (Table 2). Jacobs et al. [18] reported a monotonic decease of θ_{COOH} with increasing Pt loading (0.5–5.0 wt.%) on Pt/CeO_2 for the WGS at 250 °C, in agreement with the present results ("C-pool", Table 2). The authors explained this behavior as due to the increased reaction rate per gram basis by increasing Pt loading, as discussed before; therefore, formate (active intermediate) surface coverage is expected to decrease.

Based on the SSITKA-MS results presented in Fig. 7a, the rate of $H_2(g)$ formation appears to be larger than that of $D_2(g)$ by a factor of about 2.2. This result implies the existence of a normal kinetic isotopic effect (NKIE), where an elementary reaction step associated with the breaking/formation of a chemical bond that involves H can be considered as rate-determining step. As will be presented and discussed below (Section 3.5.4), the "redox" mechanism largely predominates over the "associative formate with –OH group regeneration" mechanism for the present Pt/CeO_2 catalysts at 300 °C. Therefore, it is suggested that O–H bond breaking producing mobile H species and/or water dissociation on surface oxygen vacant sites of ceria must be considered as the main rate-determining elementary reaction steps. On the other hand, C–H bond breaking in the formate species, which is a minor intermediate, can be considered as a rate-limiting step in the respective "associative formate with –OH group regeneration" reaction path [74].

3.5.2. SSITKA-DRIFTS

In situ DRIFTS spectra recorded in the 3000–1250 cm^{-1} range on the 0.1 wt.% Pt/CeO_2 catalyst during SSITKA-DRIFTS studies of the WGS reaction at 300 °C are presented in Fig. 8. The 3000–2750 cm^{-1} range (Fig. 8a) corresponds to vibrational modes of adsorbed formate, –COOH (νCH and δCH + νOCO_{asym}), the 2100–1850 cm^{-1} range (Fig. 8b) to adsorbed CO on Pt [60,66,75–78], and the 1650–1250 cm^{-1} range (Fig. 8c) to the O–C–O stretching vibrational mode of formate, carbonate or carboxylate species [18,64,66–70,73]. The various infrared bands observed in Fig. 8c under the $^{12}CO/H_2O$ (solid line spectra) and $^{13}CO/H_2O$ (dashed line spectra) feed gas streams were obtained following appropriate deconvolution and curve fitting procedures [32,36]. In Fig. 8b (solid line spectrum), the strong infrared band centered at 2060 (band 1) and the very weak one at 1966 cm^{-1} (band 2) correspond to two kinds of linear adsorbed CO on Pt [60,66,75–78]. These two IR bands gave the red isotopic shift. The IR bands recorded at 1577 (band 1) and 1375 cm^{-1} (band 4) under the $^{12}CO/H_2O$ gas mixture are assigned to OCO_{as} and OCO_s vibrational modes of formate,

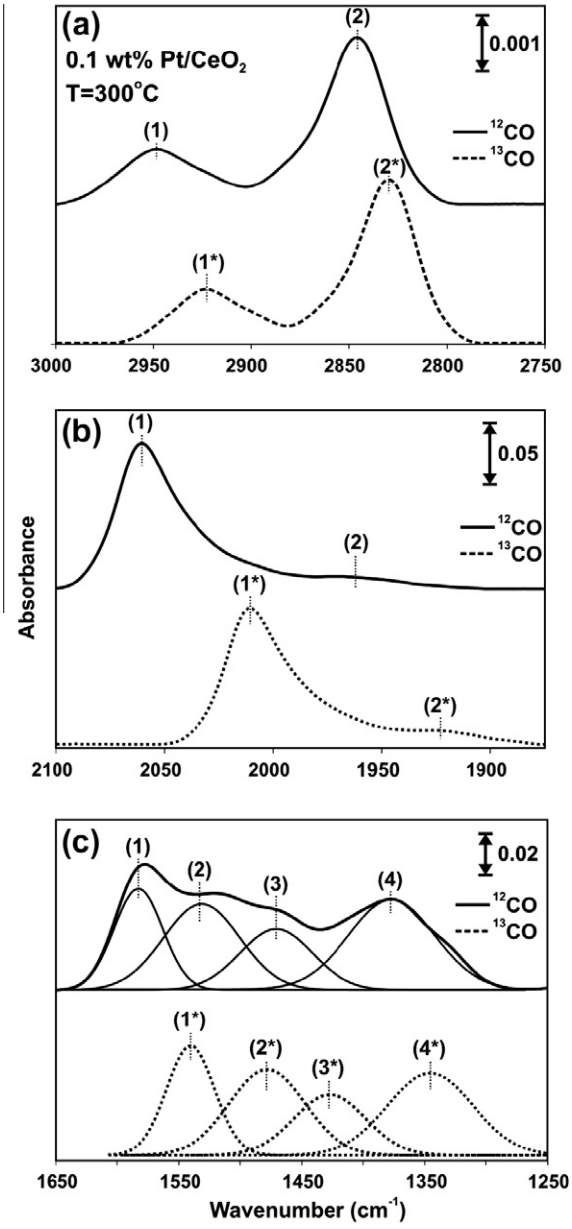

Fig. 8. *In situ* DRIFTS spectra recorded in the (a) 3000–2750 cm^{-1}, (b) 2100–1850 cm^{-1}, and (c) 1650–1250 cm^{-1} range over 0.1 wt.% Pt/CeO_2 under SSITKA WGS reaction conditions at 300 °C in 3 vol.% ^{12}CO/10 vol.% H_2O/Ar/He (solid spectra) and 3 vol.% ^{13}CO/10 vol.% H_2O/Ar (dashed spectra) feed gas mixtures. Deconvolution and curve fitting of recorded IR spectra (c) are also shown.

whereas the IR bands centered at 1530 (band 2) and 1470 cm^{-1} (band 3) to carboxylates and unidentate carbonates, respectively (Fig. 8c). The IR bands centered at 2948 and 2847 cm^{-1} (Fig. 8a, solid line spectrum) are due to νCH and δCH + νOCO_{as} vibrational modes of adsorbed –COOH on CeO_2 [18,64,66–70,73].

After the new steady state under the isotopic gas mixture of $^{13}CO/H_2O$ was reached (Fig. 8a–c, dashed line spectra), all the observed IR bands under the $^{12}CO/H_2O$ gave the red isotopic shift upon replacing the ^{12}C with ^{13}C in the "carbon-path" of the WGS reaction. *In situ* SSITKA-DRIFTS spectra were also recorded over the 0.6 and 2.0 wt.% Pt/CeO_2 catalysts, where no additional IR bands that could be assigned to different adsorbed species except those observed over the 0.1 wt.% Pt/CeO_2 catalyst (Fig. 8) were noticed.

The above-described SSITKA-DRIFTS experimental results could lead to the conclusion that at least one of the formate, carbonate, or

carboxylate adsorbed species formed at the metal–support interface as discussed before are found in the "carbon-path" of the WGS reaction; all these species provided the red isotopic shift. Adsorbed CO should be considered as a precursor intermediate for the formation of formate, carbonate, or carboxylate, and therefore, at least one of the observed linear adsorbed CO on platinum (Fig. 8b) must be considered as an active reaction intermediate. Considering that formate species could potentially be a true active intermediate, as it could first be suggested by SSITKA-DRIFTS (Fig. 8a), we have previously reported [36] that if the following elementary reaction step:

$$\text{CO-s}_1 + \text{OH-s}_2 \leftrightarrow \text{COOH-s}_1, \text{s}_2 \quad (2)$$

is considered to be a reversible one, and considering that formate species do not further react to produce CO_2 and H_2 (inactive or spectator), then during the $^{13}CO/H_2O$ switch formate is expected to be labeled as $^{13}COOH$, thus a red isotopic shift would be recorded, as it was observed (Fig. 8a and c); in Eq. (2) s_1 is a Pt site at the metal–support interface, and s_2 is an adjacent surface lattice oxygen atom to the surface Pt atom, the former accommodating an H atom (–OH group). Therefore, based only on the SSITKA results, one cannot conclusively decide whether formate could be considered as a true active intermediate.

Meunier et al. [72] were the first to determine the surface concentration (μmol/g) of formate species formed under WGS reaction conditions over Au/Ce(La)O_2 in the 155–200 °C range, which allowed them to model the SSITKA exchange curve of formate from which the rate constant (k, s^{-1}) of its decomposition reaction toward CO_2 formation was determined, and thus the rate under WGS reaction conditions could be calculated. The latter was compared to the overall WGS reaction rate, which was found to be small enough. Thus, formate was excluded from being a major reaction intermediate. In the following sections, we demonstrate that even though the decomposition reaction of formate toward CO_2(g) and H-s_1 formation is largely enhanced in the presence of water atmosphere, when compared to that under He, this decomposition rate is significantly smaller than the rate of reaction of adsorbed CO with water via a "redox" mechanism. This was made possible by the design of a novel transient isotopic experiment to be presented in Section 3.5.4.

3.5.3. Transient kinetic DRIFTS experiments

Fig. 9a and b presents DRIFTS spectra in the 2100–2030 and 3000–2750 cm^{-1} range, respectively, recorded under H_2O/He following the switch 3 vol.% CO/10 vol.% H_2O/He (300 °C, 30 min) → 10 vol.% H_2O/He (300 °C, t). It is clearly seen that the integral band intensity progressively decreases with time on stream in H_2O/He for both adsorbed formate and linear CO species. It should be noted that during the H_2O/He treatment of the catalyst, the gas effluent from the DRIFTS cell was also connected to the mass spectrometer, where production of CO, CO_2, and H_2 was noticed. On the other hand, following the switch CO/H_2O (WGS) → He (t) (see Section 2.6), the mass spectrometry analysis of the exit gas stream from the DRIFTS cell revealed only the formation of CO, where the rate of decrease in the IR band intensities of both formate and linear CO was smaller (not shown) compared to the previous case (Fig. 9).

3.5.3.1. CO/H_2O → He (t) switch. Based on the above-mentioned results, it is considered that adsorbed linear CO formed during the WGS reaction follows a first-order desorption kinetics, and dissociation of adsorbed COOH-s_1,s_2 into CO(g) and OH-s_2 can also be described by a first-order kinetics. The following elementary reaction steps and material balance equations can then be written:

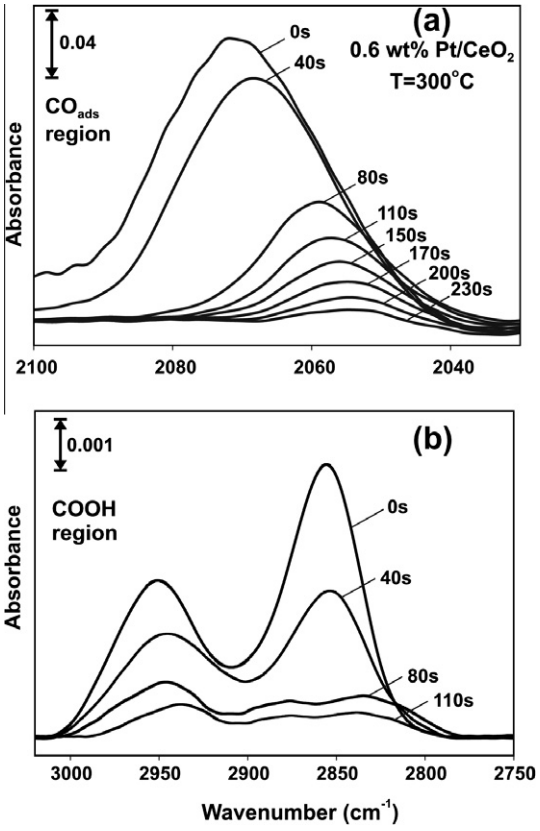

Fig. 9. *In situ* DRIFTS spectra recorded during the switch 3 vol.% CO/10 vol.% H_2O/He (300 °C, 30 min) → 10 vol.% H_2O/He (300 °C, t) for t = 0–230 s in the (a) 2100–2030 cm^{-1} and (b) 3000–2750 cm^{-1} range over the 0.6 wt.% Pt/CeO_2 catalyst.

CO balance:

$$\text{CO-s}_1 \rightarrow \text{CO}(g) + \text{s}_1 \qquad (k_{\text{des}}^{\text{CO}}) \quad (3)$$

$$d\theta_{\text{CO}}/dt = -k_{\text{des}}^{\text{CO}}\theta_{\text{CO}} \quad (4)$$

Formate balance:

$$\text{COOH-s}_1, \text{s}_2 \rightarrow \text{CO(g)} + \text{OH-s}_2 \qquad (k_{\text{dis}}^{\text{COOH}}) \quad (5)$$

$$d\theta_{\text{COOH}}/dt = -k_{\text{dis}}^{\text{COOH}}\theta_{\text{COOH}} \quad (6)$$

where: $k_{\text{dis}}^{\text{COOH}}$ is the dissociation rate constant of formate into CO(g) and OH-s_2, and $k_{\text{des}}^{\text{CO}}$ is the desorption rate constant of adsorbed CO.

3.5.3.2. CO/H_2O → H_2O/He (t) switch. It is considered that under the H_2O/He treatment, adsorbed CO can undergo simultaneously desorption and reaction (WGS), whereas adsorbed formate can undergo dissociation into CO-s_1 and OH-s_2 and reaction into CO_2(g) and H-s_1 described by Eq. (9) with the same kinetics as under the WGS reaction conditions:

$$\text{CO-s}_1 + \text{OH-s}_2 \rightarrow \text{COOH-s}_1, \text{s}_2 \qquad (k_1) \quad (7)$$

$$\text{COOH-s}_1, \text{s}_2 \rightarrow \text{CO-s}_1 + \text{OH-s}_2 \qquad (k_2) \quad (8)$$

$$\text{COOH-s}_1, \text{s}_2 \rightarrow \text{CO}_2(g) + \text{H-s}_1 \qquad (k_3) \quad (9)$$

where k_1 and k_2 are the rate constants, respectively, of the forward and backward elementary steps of formate formation and decomposition, Eqs. (7) and (8), respectively, while k_3 is the rate constant of formate decomposition into CO_2(g) and H-s_1 (Eq. (9)). The following material balance equations then apply:

CO-s_1 balance:

$$-d\theta_{\text{CO-s}_1}/dt = k_{\text{des}}^{\text{CO}}\theta_{\text{CO-s}_1} + k_1\theta_{\text{OH-s}_2}\theta_{\text{CO-s}_1} - k_2\theta_{\text{COOH-s}_1,s_2} \quad (10)$$

Adsorbed formate balance:

$$-d\theta_{\text{COOH}}/dt = k_3\theta_{\text{COOH-s}_1,s_2} + k_2\theta_{\text{COOH-s}_1,s_2} - k_1\theta_{\text{OH-s}_2}\theta_{\text{CO-s}_1} \quad (11)$$

We consider here that under the H_2O/He switch, the rate of formate dissociation into CO_2(g) and H-s_1 is significantly larger than the rate of its formation (no CO present in the gas phase) and dissociation into CO-s_1 and OH-s_2. Therefore, the last term of the right-hand side of Eqs. (10) and (11) could be neglected. After solving the first-order linear differential Eqs. (4), (6), (10), and (11), the following relationships can be obtained:

(a) CO/H_2O → He (t) gas switch:

$$\ln\frac{A[\theta_{\text{CO}}(t)]}{A[\theta_{\text{CO}}(t=0)]} = -k_{\text{des}}^{\text{CO}}\cdot t \quad (12)$$

$$\ln\frac{A[\theta_{\text{COOH}}(t)]}{A[\theta_{\text{COOH}}(t=0)]} = -k_{\text{dis}}^{\text{COOH}}\cdot t \quad (13)$$

(b) CO/H_2O → H_2O/He (t) gas switch:

$$\ln\frac{A[\theta_{\text{CO}}(t)]}{A[\theta_{\text{CO}}(t=0)]} = -k_{\text{CO}}^{*}\cdot t \quad (k_{\text{CO}}^{*} = k_{\text{des}}^{\text{CO}} + k_1\theta_{\text{OH-s}_2}) \quad (14)$$

$$\ln\frac{A[\theta_{\text{COOH}}(t)]}{A[\theta_{\text{COOH}}(t=0)]} = -k_{\text{COOH}}^{*}\cdot t \quad (k_{\text{COOH}}^{*} = k_3 + k_2) \quad (15)$$

where $A_t = A[\theta_i(t)]$ is the integral absorption intensity corresponding to the concentration of linear adsorbed CO or formate at a given time t of reaction during the switch CO/H_2O → He (t) or CO/H_2O → H_2O/He (t), and $A_0 = A[\theta_i(t=0)]$ is the corresponding integral absorption intensity at t = 0 (before the switch). In Eq. (10), it is considered that under the H_2O/He gas treatment of the catalyst, the concentration of OH groups remains constant. Also, Eq. (5) is not an independent chemical equation since it is the combination of Eqs. (3) and (8). Thus, in Eq. (13), one should substitute $k_{\text{dis}}^{\text{COOH}}$ with k_2.

Fig. 10 presents plots of the left-hand side of relationships (12)–(15) versus time based on DRIFTS measurements obtained during the two gas switches previously described. Based on the slopes of the straight-lines obtained, the rate constants k_2, $k_{\text{des}}^{\text{CO}}$ and k_3 at 300 °C were estimated. These values are found to be 1.8×10^{-3}, 4.0×10^{-3}, and 2.1×10^{-2} s^{-1}, respectively. This result illustrates that COOH-s_1,s_2 species formed under the WGS reaction conditions are about ten times more active when a 10%H_2O/He gas mixture is passed over the catalyst than pure He. It is also seen that $k_3 \gg k_2$ under the WGS reaction conditions since formation of OH-s_1 is expected to be dominated rather by the water dissociative chemisorption step on ceria (see Section 3.7) than by formate dissociation (Eq. (8)). Shido and Iwasawa [21] reported a ratio of $k_3/k_{\text{dis}}^{\text{COOH}} = 100$ at 170 °C on Rh/CeO_2, whereas Jacobs and Davis [73] reported that co-adsorbed H_2O accelerated the rate of formate decomposition toward dehydrogenation than dehydration reaction over M/CeO_2 catalysts. These findings are in harmony with the results shown in Fig. 10 described above.

3.5.4. "Redox" vs "associative formate with –OH group regeneration" mechanisms

The transient isotopic experiment described in Section 2.7 was designed and performed for the first time to our knowledge, to conclude whether formate is a major reaction intermediate in the WGS reaction path on a supported metal catalyst, and at the same time to quantitatively determine the extent of participation of adsorbed CO via the "redox" mechanism and that of formate via an "associative formate with –OH group regeneration" mechanism. Fig. 11a shows the transient response curves of H_2, $^{12}CO_2$ and $^{13}CO_2$ obtained at the switch from 3 vol.% ^{13}CO/Ar to 10 vol.% H_2O/Ar gas mixture over the 0.6 wt.%Pt/CeO_2 catalyst at 300 °C after steady-state WGS reaction was achieved. The evolution of

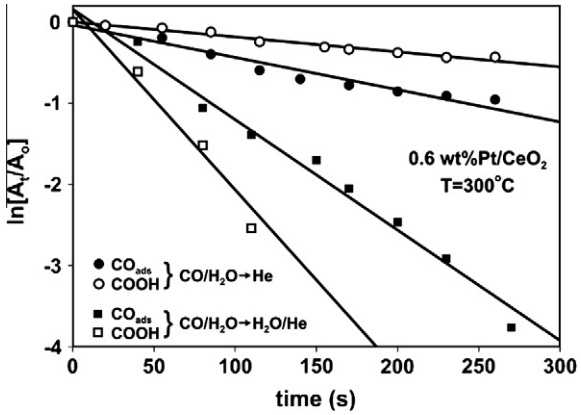

Fig. 10. Kinetic analysis of the DRIFTS spectra associated with linear CO and formate species recorded during the switch: (a) 3 vol.% CO/10 vol.% H_2O/He (30 min, 300 °C) → He (300 °C, t), and (b) 3 vol.% CO/10 vol.% H_2O/He (30 min, 300 °C) → 10 vol.% H_2O/He (300 °C, t) over the 0.6 wt.% Pt/CeO_2 catalyst according to what described in Section 3.6.3. Line slopes: -○-: k_2; -●-: $k_{\text{des}}^{\text{CO}}$; -■-: $k_{\text{des}}\text{CO} + k_1\theta_{\text{OH}}$; -□-: $k_2 + k_3$.

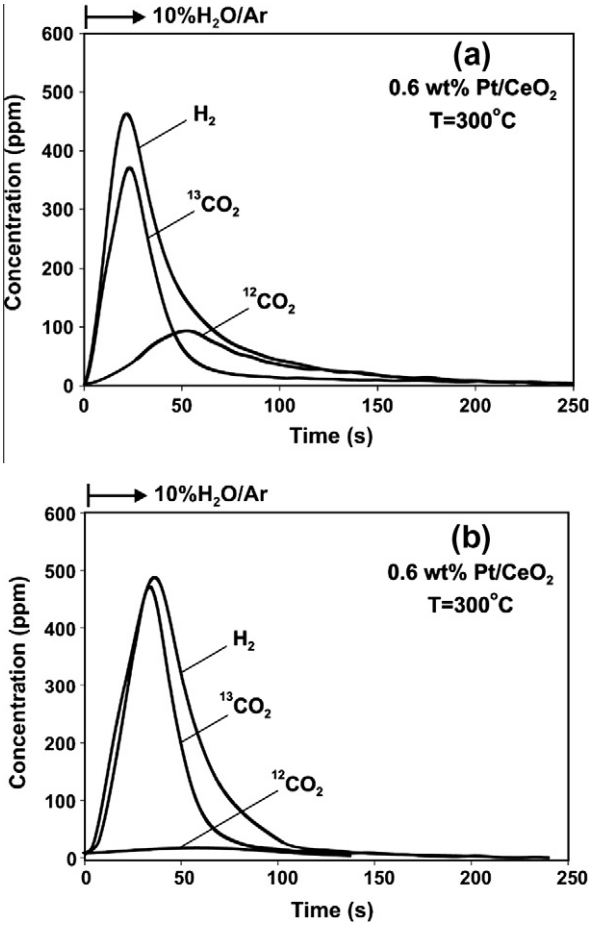

Fig. 11. (a) Transient response curves of H_2, $^{12}CO_2$, and $^{13}CO_2$ obtained on the 0.6 wt.% Pt/CeO_2 catalyst at 300 °C according to the following gas delivery: 3 vol.% ^{12}CO/10 vol.% H_2O/Ar (300 °C, 30 min) → 3 vol.% ^{13}CO/Ar (300 °C, 3 min) → 10 vol.% H_2O/Ar (300 °C, t). (b) Transient response curves of H_2, $^{12}CO_2$, and $^{13}CO_2$ obtained on the 0.6 wt.%Pt/CeO_2 catalyst at 300 °C according to the following gas delivery: 900 ppm $^{12}CO_2$/Ar (300 °C, 20 min) → 3 vol.% ^{13}CO/Ar (300 °C, 3 min) → 10 vol.% H_2O/Ar (300 °C, t).

$^{13}CO_2$ corresponds to the reaction of adsorbed ^{13}CO with water, where the former had replaced the adsorbed ^{12}CO formed under WGS upon the ^{13}CO/Ar gas treatment. On the other hand, the evolution of $^{12}CO_2$ response corresponds to the reaction of adsorbed $^{12}COOH$ species with water, the latter formed also under WGS, but the carbonyl of which was not exchanged under the ^{13}CO/Ar gas treatment [79]. It is important to state here that based on the DRIFTS results shown in Fig. 10, the extent of decomposition of $^{12}COOH$ under the ^{13}CO/Ar gas treatment is very small. By integrating the $^{13}CO_2$ and $^{12}CO_2$ responses (Fig. 11a), one is able to estimate the amounts of adsorbed CO and –COOH species formed under WGS and which reacted with water under the H_2O/Ar gas treatment. The latter quantities were found to be 8.5 μmol g^{-1} (θ = 0.74, based on Pt_s) and 4.4 μmol g^{-1} (θ = 0.38, based on Pt_s), while the amount of H_2 formed was 15 μmol g^{-1}. It is seen that the latter amount is close to the sum of the quantities of CO_2's, in agreement with the stoichiometry of WGS reaction via these two intermediate species. The small difference in the material balance appeared can be justified as due to some readsorption of produced CO_2's on the catalyst surface at 300 °C.

Fig. 11a illustrates that the shape and position of the peak maxima of $^{13}CO_2$ and $^{12}CO_2$ transient isotopic response curves are largely different. In fact, the initial transient formation rate (t_M = 24 s at peak maximum) of $^{13}CO_2$ is larger by a factor of 3.9 compared to the maximum rate of $^{12}CO_2$ formation appeared at t_M = 53 s. Considering the fact that the initial surface concentration of adsorbed CO and formate differ only by a factor of two, it is conclusive that based on the initial rates, the rate of CO_2 formation via the "redox" mechanism largely controls the overall WGS reaction rate. This analysis even though does not estimate individual steady-state rates of the two parallel reaction paths, those of adsorbed CO via "redox" and of –COOH via an "associative formate with –OH group regeneration" as shown in Scheme 1a and b, respectively, to be discussed next, it should be considered as an alternative powerful tool to those proposed earlier by Meunier [72] and Oyama et al. [80], which allows to investigate in a quantitative manner the contribution of formate species in the overall WGS reaction rate. It is interesting to note that the surface coverage of adsorbed CO and formate determined by the isotopic experiment presented in Fig. 11a is larger than the size of the "C-pool" determined from SSITKA studies. This result suggests that not all adsorbed CO and formate species participate in the WGS under steady state. It appears from these results that as long as CO is removed from the gas phase, and adsorbed CO starts to react with water, an increasing concentration of empty sites on Pt is formed which accelerates the rate of formate decomposition on Pt (Rate $_{COOH} = k\theta_{COOH}\cdot\theta_s$).

Fig. 11b presents the results of another transient isotopic experiment designed in order to exclude the possibility that the $^{12}CO_2$ transient response shown in Fig. 11a was the result of any reaction of adsorbed carbonate species with water upon the H_2O/Ar gas switch. The catalyst was first treated with 900 ppm $^{12}CO_2$/Ar gas at 300 °C for 20 min, purged with He for 3 min, and the gas flow was then switched to the 3 vol.% ^{13}CO/Ar for 3 min, as in the experiment presented in Fig. 11a. The feed was then switched to 10 vol.% H_2O/Ar and the transient responses of H_2, $^{12}CO_2$, and $^{13}CO_2$ recorded are presented in Fig. 11b. It is seen that practically no formation of $^{12}CO_2$ was obtained, whereas the $^{13}CO_2$ response is due to the reaction of adsorbed ^{13}CO with water. It is also noted that upon the ^{13}CO/Ar gas treatment, no ^{12}CO was formed, excluding, therefore, the exchange of carbonyl in $^{12}CO_3^{2-}$ with gas phase ^{13}CO.

3.6. Probing the participation of labile oxygen of ceria support in the WGS reaction

The contribution of labile oxygen of CeO_2 support during the WGS reaction over the 0.6 wt.% Pt/CeO_2 catalyst (see $^{13}CO_2$ response in Fig. 11a) was probed by another isotopic experiment described in Section 2.8. Fig. 12 presents transient response curves of $C^{16}O_2$, $C^{16}O^{18}O$, and $C^{18}O_2$ obtained under the 3 vol.% CO/10 vol.% H_2O/Ar gas mixture according to the following gas sequence: 5 vol.% $^{18}O_2$/He (600 °C, 30 min) → He, cool down to 80 °C → H_2 (1 bar, 80 °C, 20 min) → Ar (300 °C, 20 min) → 3 vol.% CO/10 vol.% H_2O/Ar (300 °C, t). Integration of the $C^{18}O^{16}O$ and $C^{18}O_2$ response curves based on the material balance equation described [81] provides the amount of ^{18}O (μmol O g^{-1}) present in the CeO_2 support and which participated in the "carbon-path" of WGS reaction

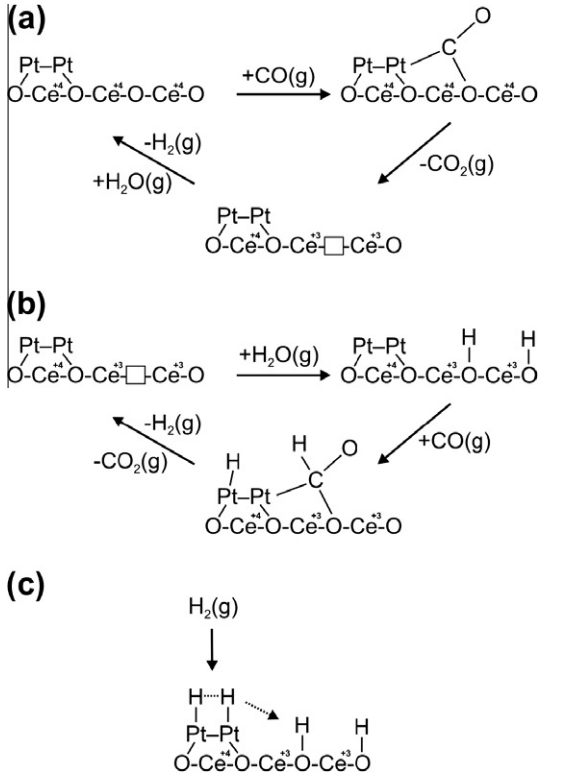

Scheme 1. Proposed "redox" (a) and "associative formate with –OH group regeneration" (b) mechanisms operated in the WGS reaction over ceria-supported platinum catalysts at 300 °C, and (c) suggested hydrogen spillover mechanism from Pt to ceria forming –OH groups during WGS over Pt/CeO_2 catalysts.

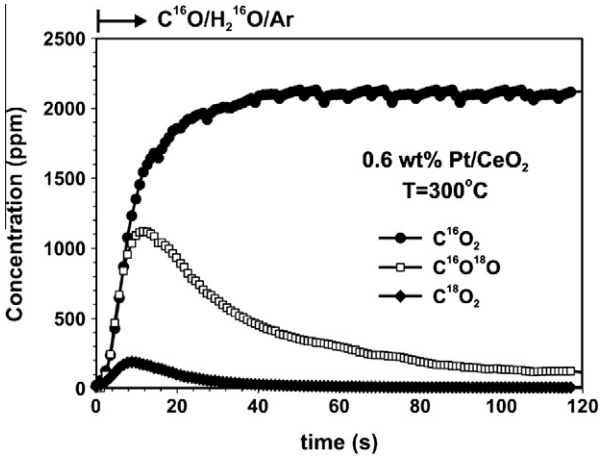

Fig. 12. Transient response curves of $C^{16}O_2$, $C^{16}O^{18}O$ and $C^{18}O_2$ obtained during $^{18}O/^{16}O$ isotope exchange at 600 °C followed by WGS reaction ($C^{16}O/H_2^{16}O$/He) over the 0.6 wt.% Pt/CeO_2 catalyst at 300 °C according to the procedures described in Section 2.8.

under the given transient conditions. This quantity was estimated to be 41.9 μmol^{18}O g_{cat}^{-1} or 1.4 equivalent monolayers of surface Pt (θ_0 = 1.4). This result illustrates clearly the participation of lattice oxygen of ceria support to the "carbon-path" of the WGS since CeO_2 was the only source of ^{18}O according to the experiment designed. It is to be remarked that the estimated concentration of ^{18}O which resulted in the CO_2 formation is significantly larger than the surface concentration of the truly active –OH and –COOH intermediates derived by the SSITKA experiment (Table 2, 2nd and 3rd columns). This is due to the fact that under the ^{16}O/^{18}O isotopic exchange performed at 600 °C, subsurface lattice ^{16}O has also been exchanged with ^{18}O [82]. Under WGS reaction at 300 °C, diffusion of this subsurface ^{18}O toward the ceria surface is possible. Also, it is possible that under steady-state WGS, the accessible number density of labile oxygen on ceria accommodating –COOH species might be lower when compared to the fresh state of the catalyst (Fig. 12). It should be noted that based on an isothermal H_2 titration experiment (1 vol.% H_2/He) performed at 80 °C, following catalyst oxidation at 600 °C, reduction of PtO_2 was complete within 20 min as evidenced by the material balance performed.

3.7. Proposed WGS reaction mechanisms on Pt/CeO_2 at 300 °C

Two mechanistic paths are widely considered in the literature for the WGS reaction over Pt/CeO_2 catalysts [11–13,18–20]: a "*redox*" and an "*associative formate*" mechanism. In the first mechanism (Scheme 1a), CO adsorbs on the Pt surface which then diffuses toward the metal–support interface and reacts with support lattice oxygen to form CO_2(g). Water adsorbs and dissociates mainly on the reduced Ce^{3+} support sites, thus re-oxidizing the support sites and producing H_2(g). According to this mechanism, the active "carbon-containing" intermediates include adsorbed CO on Pt and adsorbed CO associated with Pt and O sites of support (e.g., CO_2^- species) as depicted in Scheme 1a. In the second mechanism, –OH groups formed by water dissociation on an oxidized support surface leads to a formate reaction intermediate, the decomposition of which by the aid of metal leads to the CO_2 and H_2(g) formation.

In Scheme 1b, a combination of these two mechanistic paths is suggested to operate on Pt/CeO_2 based on the present SSITKA and other transient isotopic experiments performed (Figs. 7–12, Table 2). According to Scheme 1b, this mechanism is named "*associative formate with –OH group regeneration*", since water dissociation at oxygen vacancies does not change the formal oxidation state of cerium from Ce^{3+} to Ce^{4+}. It implies that a formate intermediate is formed via the participation of CO and labile oxygen of support at the ceria–Pt interface. This formate species with the interaction of an adjacent adsorbed H on Pt is not stable and decomposes, producing CO_2(g) and H_2(g) and leaving oxygen vacancies on the ceria support. Water then dissociates at these oxygen vacancies producing hydroxyl groups on the ceria surface ("H source"). It should be noted that the presence of oxygen vacancies on fully oxidized ceria is controlled by the rate of their formation via reaction of adsorbed CO on Pt with labile oxygen at the ceria–Pt interface and the rate of their replenishment by water dissociation.

According to the results of the transient isotopic experiment presented in Fig. 11 and of the specific kinetic rate dependence on Pt particle size (Fig. 6b), the "redox" mechanism shown in Scheme 1a is prevailing over the "associative formate with –OH group regeneration" mechanism irrespective of the Pt particle size. In Scheme 1c, it is also suggested that reduced ceria sites along the Pt–ceria interface could be created by the presence of hydrogen product via a spillover mechanism. As proposed earlier based on experimental evidence [18], the Pt particle size has a significant impact on the ease of ceria reduction at the Pt–ceria interface, where an increasing activity per gram of catalyst basis was observed with increasing Pt loading and particle size, in harmony with the present catalytic results (Fig. 4). The partial reduction of ceria is also necessary for generating bridging –OH groups on the surface of ceria, which serve as the active sites for the –COOH intermediate formation. The fact that a NKIE for D was observed (Fig. 7a), and that the small change in the apparent activation energy of the WGS reaction by 1–2 kcal/mol for Pt particle sizes between 1.3 and 8.0 nm could explain the kinetic results of Fig. 6b as discussed before, it is suggested that both an increase in the number density of required Ce^{3+}–□–Ce^{3+} sites for water dissociation and the lowering of activation energy for water dissociation on these sites with increasing Pt particle size can explain in a satisfactory manner the strong dependence of the specific rate of WGS reaction per length of perimeter of Pt–ceria interface with the Pt particle size. The importance of the *site reactivity* of Pt and oxygen atoms located along the Pt/CeO_2 and Pt/SiO_2-alkali-promoted interfaces was recently illustrated by Pierre et al. [22] and Zhai et al. [23]. Meunier et al. [83] reported that a switch-over from a non-formate-based to a formate-based WGS reaction mechanism might take place over a narrow temperature window (e.g., as low as 60 °C) on Pt/CeO_2. This implies that the WGS reaction mechanism on ceria-supported Pt catalysts could be influenced by the reaction conditions. They also suggested that the same surface species can be a spectator under certain reaction conditions or the main active intermediate under different reaction conditions. The present results strengthen the latter view since the "redox" mechanism on Pt/CeO_2 is largely operated at 300 °C, whereas an "associative formate" mechanism was suggested to operate at 250 °C [18].

4. Conclusions

The following conclusions can be derived from the results of the present work:

(a) The WGS reaction performed on Pt/CeO_2 catalysts (d_{Pt} = 1.3–8.0 nm) at 300 °C is suggested to be governed mainly through a "*redox*" bifunctional mechanism and to a lesser extent through the parallel "*associative formate with –OH group regeneration*" mechanism. The increase in Pt particle size results in the enhancement of density of sites for water dissociation (oxygen vacancies) within a narrow zone around the Pt nanoparticles and also to the increase in their reactivity.

(b) An experimental methodology to discriminate between the "redox" and "associative formate with –OH group regeneration" mechanisms for WGS over supported metal catalysts by a combination of transient infrared spectroscopic and isotopic studies was developed.

(c) The "carbon-containing" (linear CO, –COOH) and "hydrogen-containing" (bridging –OH, –COOH, H) *active* intermediates of the WGS were found to be justified as formed along the periphery of Pt–ceria interface, and within a narrow zone around this periphery, respectively. As the Pt particle size increases from 3.0 to 8.0 nm (or Pt loading from 0.6 to 2.0 wt.%), the surface concentration of these active species decreases, while the specific rate per length of periphery of the Pt–ceria interface (μmol cm^{-1} s^{-1}) increases linearly. On the other hand, the TOF (s^{-1}) of WGS is found to slightly only depend on Pt particle size (3.0–8.0 nm) in the temperature range of 250–300 °C.

(d) The interaction of CO (CO/He, 25 °C) with the ceria-supported Pt catalysts studied by *in situ* DRIFTS showed the formation of three kinds of adsorbed CO, namely HF-linear, LF-linear, and bridged CO. The HF-linear adsorbed CO was

found to be the least stable and desorbs at temperatures below 300 °C in He flow, while the LF-linear CO was the predominant species under WGS reaction conditions at 300 °C. This species is the active CO precursor via the main "redox" mechanism to form CO_2, and also for the formation of –COOH intermediate via the minor "associative formate with –OH group regeneration" mechanism for the present Pt/CeO_2 catalyst.

Acknowledgments

The financial support of the Cyprus Research Promotion Foundation (project ΠΕΝΕΚ/ΕΝΙΣΧ/0503/50) and the Research Committee of the University of Cyprus is gratefully acknowledged. Dr. Sergio Garcia (Instituto de Catálisis y Petroleoquimica, CSIC, Madrid, Spain) is gratefully acknowledged for the STEM measurements.

Appendix A. Supplementary material

Supplementary data associated with this article can be found, in the online version, at doi:10.1016/j.jcat.2011.01.024.

References

[1] W. McDowall, M. Eames, Energy Policy 34 (2006) 1236.
[2] F. Mueller-Langer, E. Tzimas, M. Kaltschmitt, S. Peteves, Int. J. Hydrogen Energy 32 (2007) 3797.
[3] European Hydrogen and Fuel Cell Technology Platform, Strategic Research Agenda, European Union, July 2005.
[4] A.C. Basagiannis, X.E. Verykios, Appl. Catal. A: Gen. 308 (2006) 182.
[5] S. Chernik, R. French, C. Feik, E. Chornet, Ind. Eng. Chem. Res. 41 (2002) 4209.
[6] R.D. Cortright, R.R. Davda, J.A. Dumesic, Nature 418 (2002) 964.
[7] Q. Fu, H. Saltsburg, M. Flytzani-Stephanopoulos, Science 301 (2003) 935. and references therein.
[8] D.S. Newsome, Catal. Rev. Sci. Eng. 21 (1980) 275.
[9] R. Burch, Phys. Chem. Chem. Phys. 8 (2006) 5483.
[10] F.C. Meunier, Catal. Today 155 (2010) 164 (Review).
[11] T. Bunluesin, R.J. Gorte, G.W. Graham, Appl. Catal. B: Environ. 15 (1998) 107.
[12] R.J. Gorte, S. Zhao, Catal. Today 104 (2005) 18.
[13] S. Hilaire, X. Wang, T. Luo, R.J. Gorte, J. Wagner, Appl. Catal. A: Gen. 215 (2001) 271.
[14] Y. Li, Q. Fu, M. Flytzani-Stephanopoulos, Appl. Catal. B: Environ. 27 (2000) 179.
[15] W. Liu, M. Flytzani-Stephanopoulos, J. Catal. 153 (1995) 317.
[16] B.A.A. Silberova, G. Mul, M. Makkee, J.A. Moulijn, J. Catal. 243 (2006) 171.
[17] E. Chenu, G. Jacobs, A.C. Crawford, R.A. Keogh, P.M. Patterson, D.E. Sparks, B.H. Davis, Appl. Catal. B: Environ. 59 (2005) 45.
[18] G. Jacobs, U.M. Graham, E. Chenu, P.M. Patterson, A. Dozier, B.H. Davis, J. Catal. 229 (2005) 499.
[19] G. Jacobs, L. Williams, U. Graham, D. Sparks, B.H. Davis, J. Phys. Chem. B 107 (2003) 10398.
[20] G. Jacobs, L. Williams, U. Graham, G.A. Thomas, D.E. Sparks, B.H. Davis, Appl. Catal. A: Gen. 252 (2003) 107.
[21] T. Shido, Y. Iwasawa, J. Catal. 141 (1993) 71. and references therein.
[22] D. Pierre, W. Deng, M. Flytzani-Stephanopoulos, Top. Catal. 46 (2007) 363.
[23] Y. Zhai, D. Pierre, R. Si, W. Deng, P. Ferrin, A.U. Nilekar, G. Peng, J.A. Herron, D.C. Bell, H. Saltsburg, M. Mavrikakis, M. Flytzani-Stephanopoulos, Science 329 (2010) 1633. and references therein.
[24] K. Tamaru, Dynamic Heterogeneous Catalysis, Academic Press, New York, 1978.
[25] V.A. Matyshak, O.V. Krylov, Catal. Today 25 (1995) 1. and references therein.
[26] J. Happel, Isotopic Assessment of Heterogeneous Catalysis, Academic Press, New York, 1986.
[27] S.L. Shannon, J.G. Goodwin Jr., Chem. Reviews 95 (3) (1995) 677.
[28] M.W. Balakos, S.S.C. Chuang, G. Srivinas, J. Catal. 140 (1993) 281.
[29] C.O. Bennett, Adv. Catal. 44 (1999) 329. and references therein.
[30] C.N. Costa, T. Anastasiadou, A.M. Efstathiou, J. Catal. 194 (2000) 250.
[31] C.N. Costa, A.M. Efstathiou, J. Phys. Chem. B 108 (2004) 2620.
[32] B.C. Smith, Fundamentals of Fourier Transform Infrared Spectroscopy, CRC Press, 1996.
[33] K. Polychronopoulou, C.N. Costa, A.M. Efstathiou, Appl. Catal. A: Gen. 272 (2004) 37.
[34] G.F. Froment, K.B. Bischoff, Chemical Reactor Analysis and Design, John Wiley & Sons Inc., New York, 1979.
[35] A.M. Efstathiou, X.E. Verykios, Appl. Catal. A: Gen. 151 (1997) 109.
[36] C.M. Kalamaras, G.G. Olympiou, A.M. Efstathiou, Catal. Today 138 (2008) 228.
[37] G.G. Olympiou, C.M. Kalamaras, C.D. Zeinalipour-Yazdi, A.M. Efstathiou, Catal. Today 127 (2007) 304.
[38] J. Sirita, S. Phanichphant, F.C. Meunier, Anal. Chem. 79 (2007) 3912.
[39] S. Bernal, M.A. Cauqui, G.A. Cifredo, J.M. Gatica, C. Larese, J.A.P. Omil, Catal. Today 29 (1996) 77.
[40] P.J. Levy, M. Primet, Appl. Catal. 70 (1991) 263.
[41] G.S. Zafiris, R.J. Gorte, Surf. Sci. 276 (1992) 86.
[42] D.M. Collins, W.E. Spicer, Surf. Sci. 69 (1977) 85.
[43] M. Che, C.O. Bennett, Adv. Catal. 36 (1989) 55.
[44] A. Carlsson, A. Puig-Molina, T.V.W. Janssens, J. Phys. Chem. B 110 (2006) 5286.
[45] (a) J.S. Rieck, A.T. Bell, J. Catal. 85 (1984) 143;
(b) Y.-J. Huang, J. Xue, J.A. Schwarz, J. Catal. 109 (1988) 396;
(c) R.J. Gorte, J. Catal. 75 (1982) 164.
[46] A.M. Efstathiou, C.O. Bennett, J. Catal. 124 (1990) 116. and references therein.
[47] R. Barth, R. Pitchai, L.R. Anderson, X.E. Verykios, J. Catal. 116 (1989) 61.
[48] A. Bourane, O. Dulaurent, D. Bianchi, J. Catal. 196 (2000) 115.
[49] N.W. Cant, R.A. Donaldson, J. Catal. 71 (1981) 320.
[50] D.M. Haalant, F.L. Williams, J. Catal. 110 (1982) 319.
[51] Y.E. Li, D. Boeeker, R.D. Gonzalez, J. Catal. 110 (1988) 319.
[52] O. Pozdnyakova, D. Teschner, A. Wootsch, J. Krohnert, B. Steinhauer, H. Sauer, L. Toth, F.C. Jentoft, A.K. Gericke, Z. Paal, R. Schlögl, J. Catal. 237 (2006) 1.
[53] M. Primet, J.M. Basset, M.V. Mathieu, M. Prettre, J. Catal. 29 (1973) 213.
[54] J. Rasko, J. Catal. 217 (2003) 478.
[55] O.P. Tellinger, D. Teschner, J. Krohnert, F.C. Jentoft, A.K. Gericke, R. Schlögl, A. Wootsch, J. Phys. Chem. C 111 (2007) 5426.
[56] D. Tibiletti, A. Goguet, D. Reid, F.C. Meunier, R. Burch, Catal. Today 113 (2006) 94.
[57] C.M.Y. Yeung, F. Meunier, R. Burch, D. Thompsett, S.C. Tsang, J. Phys. Chem. B 110 (2006) 8540.
[58] M. Primet, J. Catal. 88 (1984) 273.
[59] P. Panagiotopoulou, D.I. Kondarides, Catal. Today 112 (2006) 49.
[60] P. Panagiotopoulou, J. Papavasiliou, G. Avgouropoulos, T. Ioannides, D.I. Kondarides, Chem. Eng. J. 134 (2007) 16.
[61] B.L. Mojet, J.T. Miller, D.E. Ramaker, D.C. Koningsberger, J. Catal. 186 (1999) 373.
[62] A.-P. Jia, S.-Y. Jiang, J.-Q. Lu, M.-F. Luo, J. Phys. Chem. C 114 (2010) 21605.
[63] Y.M. Choi, H. Abernathy, H.-T. Chen, M.C. Lin, M. Liu, Chem. Phys. Chem. 7 (2006) 1957.
[64] G. Jacobs, P.M. Patterson, U.M. Graham, A.C. Crawford, B.H. Davis, Int. J. Hydrogen Energy 30 (2005) 1265.
[65] G. Jacobs, P.M. Patterson, U.M. Graham, D.E. Sparks, B.H. Davis, Appl. Catal. A: Gen. 269 (2004) 63.
[66] G. Jacobs, P.M. Patterson, L. Williams, E. Chenu, D. Sparks, G. Thomas, B.H. Davis, Appl. Catal. A: Gen. 262 (2004) 177.
[67] G. Jacobs, S. Ricote, B.H. Davis, Appl. Catal. A: Gen. 284 (2005) 31.
[68] G. Jacobs, S. Ricote, B.H. Davis, Appl. Catal. A: Gen. 302 (2006) 14.
[69] K.G. Azzam, I.V. Babich, K. Seshan, L. Lefferts, J. Catal. 251 (2007) 153.
[70] S. Ricote, G. Jacobs, M. Milling, Y. Ji, P.M. Patterson, B.H. Davis, Appl. Catal. A: Gen. 303 (2006) 35.
[71] R. Leppelt, B. Schumacher, V. Plzak, M. Kinne, R.J. Behm, J. Catal. 244 (2006) 137.
[72] F.C. Meunier, D. Reid, A. Goguet, S. Shekhtman, C. Hardacre, R. Burch, W. Deng, M. Flytzani-Stephanopoulos, J. Catal. 247 (2007) 277.
[73] G. Jacobs, B.H. Davis, Appl. Catal. A: Gen. 333 (2007) 192.
[74] G. Jacobs, B.H. Davis, Int. J. Hydrogen Energy 35 (2010) 3522.
[75] O.S. Alexeev, S.Y. Chin, M.H. Engelhard, L. Ortiz-Soto, M.D. Amiridis, J. Phys. Chem. B 109 (2005) 23430.
[76] L.H. Little, IR Spectra of Adsorbed Species, Academic Press, New York, 1966.
[77] P. Panagiotopoulou, D.I. Kondarides, J. Catal. 260 (2008) 141.
[78] A. Yee, S.J. Morrison, H. Idriss, J. Catal. 191 (2000) 30.
[79] A.M. Efstathiou, C.O. Bennett, J. Catal. 120 (1989) 137. and references therein.
[80] J.J. Bravo-Suárez, K.K. Bando, J. Lu, M. Haruta, T. Fujitani, S.T. Oyama, J. Phys. Chem. C 112 (2008) 1115;
T. Gott, S.T. Oyama, J. Catal. 263 (2009) 359;
C. Reed, Y. Xi, S.T. Oyama, J. Catal. 235 (2005) 378.
[81] C.M. Kalamaras, P. Panagiotopoulou, D.I. Kondarides, A.M. Efstathiou, J. Catal. 264 (2009) 117.
[82] S.Y. Christou, H. Bradshaw, C. Butler, J. Darab, A.M. Efstathiou, Top. Catal. 52 (2009) 2013.
[83] F.C. Meunier, D. Tibiletti, A. Goguet, S. Shekhtman, C. Hardacre, R. Burch, Catal. Today 126 (2007) 143.